MINIREVIEW

Recent advances in Ti₃C₂Tₓ MXene-based composites for electrocatalytic applications

Minh-Hai Tran, [ID] †[a] Vo Thi Thuy Linh,†[b] Ly Tan Nhiem, [ID] †[c] Phan Khanh Thinh Nguyen [ID] *[d] and Qui Thanh Hoai Ta [ID] *[e]

Electrocatalysis is central to the development of sustainable energy conversion technologies and environmental remediation systems, yet the rational design of high-performance, cost-effective, and durable electrocatalysts remains a fundamental challenge. In recent years, MXenes, a rapidly expanding family of two-dimensional transition-metal carbides, nitrides, and carbonitrides, have emerged as a transformative class of materials owing to their metallic conductivity, tunable surface chemistry, rich termination groups, and structural versatility. These unique attributes endow MXenes with exceptional potential for a wide spectrum of electrocatalytic reactions, including the hydrogen evolution reaction, oxygen evolution reaction, and CO_2 reduction reaction. This review provides a fundamental assessment of Ti₃C₂Tₓ MXene-based electrocatalysts, encompassing synthesis strategies, surface and termination chemistry, and structure–performance relationships. Particular emphasis is placed on how etching routes, delamination processes, and functional group engineering govern catalytic performances. Recent advances in Ti₃C₂Tₓ MXene composites, heterostructures, and defect engineering are systematically analyzed to elucidate synergistic effects and catalytic enhancement mechanisms. Furthermore, the challenges hindering practical implementation, such as oxidation instability, restacking, ion transport limitations, and the need for scalable manufacturing, are discussed. By integrating experimental insights with theoretical modeling and emerging data-driven approaches, this review outlines future research directions and design principles aimed at bridging the gap between laboratory-scale performance and industrial deployment. Overall, this work is expected to establish Ti₃C₂Tₓ MXene-based composites as a versatile and continuously evolving platform for next-generation electrocatalysis, while providing a strategic roadmap for their rational design and development in electrocatalytic applications.

1. Introduction

In contemporary society, increasing concerns over the energy crisis and global warming have emerged, largely driven by rapid population growth and industrialization. To address these pressing challenges, it is imperative to explore alternative energy sources to replace fossil fuels and to develop strategies that mitigate environmental degradation.[1–3] The scale-up

synthesis of green energy carriers, including ammonia, solar, and hydrogen energy, as alternatives to fossil fuels, is strongly encouraged. In particular, green energy conversion strategies such as electrochemical water splitting and carbon dioxide capture and conversion are central to achieving carbon neutrality. Among the potential technologies, electrocatalysis has emerged as a rising star in the field of energy storage and conversion, playing a crucial role in promoting sustainable development. However, conventional electrocatalysts based on noble metals (Ir, Au, and Pt) suffer from high cost, limited availability, and poor stability and durability under harsh operating conditions, which severely restrict their large-scale application at the pilot level.[4,5] Therefore, the development of low-cost electrocatalysts with high efficiency is imperative to advance the new era of green development and sustainability.[6–8] Material-based catalysis has garnered significant interest within the scientific community for its potential in energy harvesting, particularly in the development of high-performance electrocatalysts. Materials such as graphene, MXenes, conductive polymers, and carbon-based structures have been extensively investigated for their applications in metal-ion batteries (*e.g.*,

ᵃDepartment of Materials and Chemical Engineering, Concordia University, 1515 Ste. Catherine St. W., Montreal, QC H3G 2W1, Canada. E-mail: mis.miha@gmail.com

ᵇFaculty of Natural Science Education, Pham Van Dong University, Quang Ngai, Vietnam. E-mail: vttlinh@pdu.edu.vn

ᶜFaculty of Chemical and Food Technology, Ho Chi Minh City University of Technology and Education, 01 Vo Van Ngan Street, Thu Duc Ward, Ho Chi Minh City, Vietnam. E-mail: nhiemlt@hcmute.edu.vn

ᵈSchool of Chemical, Biological, and Battery Engineering, Gachon University, 1342 Seongnamdaero, Sujeong-gu, Seongnam-si, Gyeonggi-do 13120, Republic of Korea. E-mail: thinhnpk@gachon.ac.kr

ᵉInstitute of Advanced Technology, Vietnam Academy of Science and Technology, 1B TL29 Street, An Phu Dong Ward, Ho Chi Minh City 700000, Vietnam. E-mail: tathanhhoaiqui2292@gmail.com

† First author.

sodium- and lithium-ion batteries), the hydrogen evolution reaction (HER), the oxygen reduction reaction (ORR), and supercapacitors.[9–13]

MAX phases, the precursors to MXenes, possess the general formula $M_{n+1}AX_n$, where n ranges from 1 to 4. In this structure, M represents early transition metals such as chromium (Cr), titanium (Ti), hafnium (Hf), molybdenum (Mo), niobium (Nb), or vanadium(V); A is typically a group 13 or 16 element, such as aluminum (Al) or silicon (Si); and X denotes carbon and/or nitrogen.[14] The A element usually has a lower melting point than both M and X and is bonded to the M layers *via* metallic interactions.[15,16] In contrast, the bonding between M and X involves a combination of covalent, metallic, and ionic interactions, which are generally stronger than those between M and A. MXenes are synthesized by selectively etching the A layer from MAX phases, resulting in two-dimensional transition metal carbides, nitrides, or carbonitrides.[17,18] After the etching process, MXene surfaces are decorated with terminal functional groups (T_x), which play a crucial role in tailoring interfacial interactions and enabling diverse composite fabrication and applications. MXene-based composites have been widely applied in diverse fields, including biomedical applications and environmental remediation. For instance, Cu-doped MXene has been confirmed to exhibit strong antibacterial activity against *Escherichia coli* and *Staphylococcus aureus*, achieving inhibition and bacterial killing efficiencies of approximately 99%.[19] The optimized Cu-MXene generates reactive oxygen species (ROS), which damage bacterial DNA and disrupt cellular membranes. Moreover, Cu-MXene interferes with the bacterial electron transport chain, thereby inhibiting essential metabolic activities. The nanoscale size and positively charged surface of Cu-MXene play a crucial role in enhancing adhesion to bacterial cell surfaces, further improving its antibacterial effectiveness. In another study, Cu/MXene was designed for urea adsorption, exhibiting an adsorption capacity in the range of 39.3–78.6 μmol.[20] The plausible adsorption mechanism was attributed to the uniform dispersion of Cu on the MXene surface and the strong interaction between urea molecules and Cu sites, where the electron-rich oxygen atom of the carbonyl group in urea coordinates with electron-deficient Cu species. This structural feature highlights the promising potential of MXene-based materials as dialysis membranes for wastewater treatment. Cetyltrimethylammonium bromide (CTAB) and polyvinylpyrrolidone (PVP) have been incorporated with MXenes to achieve adjustable permeability in membrane-based systems.[21] The optimized composites exhibited high adsorption capacities toward organic dyes, with loading amounts of methyl orange and methylene blue reaching 108.61 and 70.05 mg g^{-1}, respectively. In the same context, PVP/MXene composites have been synthesized for energy-harvesting applications. The resulting PVP/MXene electrode exhibited a high specific capacitance of 154.6 F g^{-1} at a current density of 0.3 A g^{-1}.[22] The optimized interlayer spacing of the MXene, together with the uniform wrapping of PVP, plays a key role in increasing the number of accessible electroactive sites and enhancing electron transport within the electrode material in aqueous electrolytes.
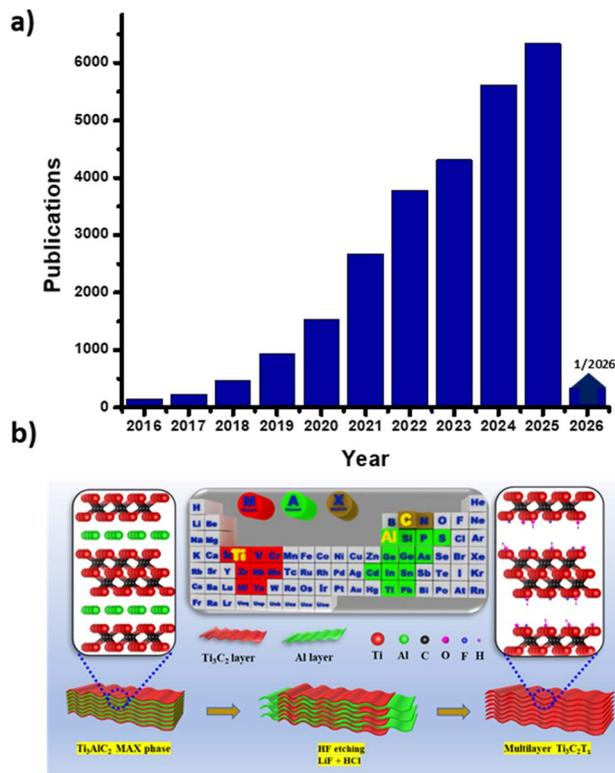

Fig. 1 Animated illustration showing (a) the evolution of MXene-related publications and (b) the fluorine-based synthesis routes for $Ti_3C_2T_x$ MXene. Reproduced from ref. 31 with permission from Elsevier, copyright 2021.

As shown in Fig. 1a, Web of Science records show a rapidly increasing number of publications focusing on MXenes and their applications, with annual outputs growing steadily. Although numerous studies have reported the electrochemical performance of MXenes in various applications,[23–26] a review that systematically summarizes and discusses the fundamental principles and recent progress in the HER, OER, and CO$_2$RR over MXenes and their derivatives is still urgently needed.

Since its discovery in 2011, $Ti_3C_2T_x$ MXene has attracted considerable attention due to its unique physicochemical properties, including a multilayered structure with abundant surface-active sites, excellent electrical conductivity, and intrinsic hydrophilicity. This review aims to elucidate the fundamental aspects of MXenes, including their synthesis methods, physicochemical properties, and potential applications. Recent advancements in the electrocatalytic applications of MXenes are highlighted, followed by a critical analysis of current findings and a forward-looking perspective on the future development of MXene-based catalysts.

2. Synthesis methods

$Ti_3C_2T_x$ MXenes are two-dimensional (2D) transition metal carbides and nitrides that show unique electrical conductivity, excellent thermal conductivity, a large surface area with abundant surface termination groups, and superior mechanical strength. The first preparation of MXenes was reported in 2011
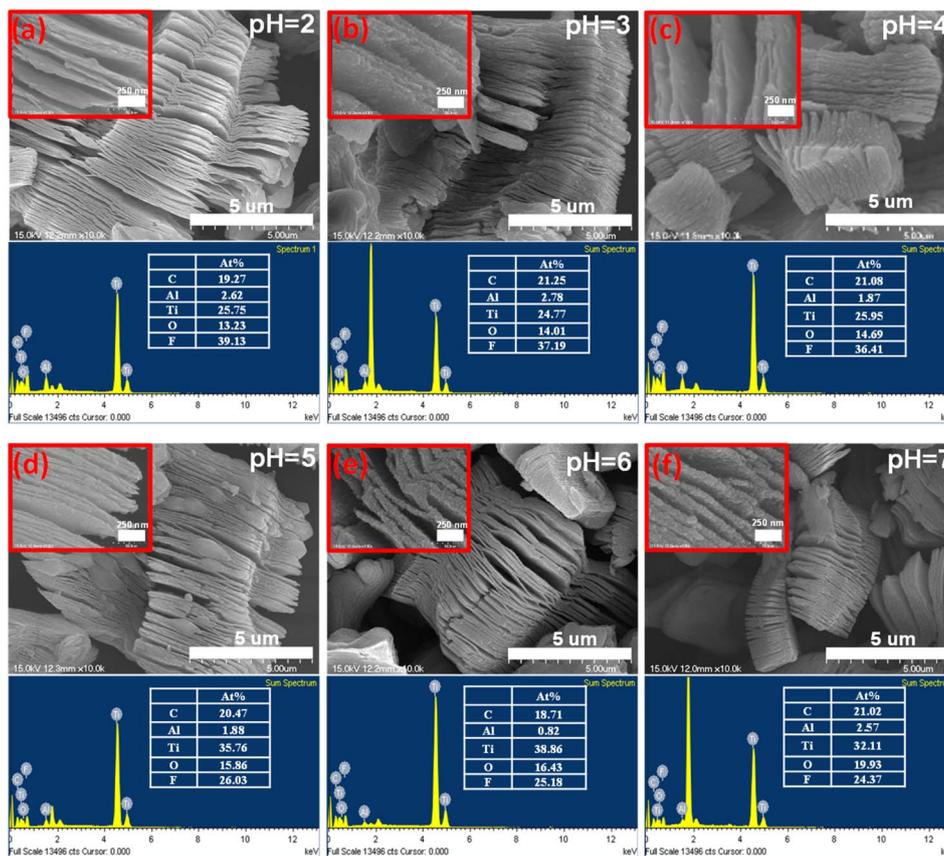
Fig. 2 (a–f) SEM images of $Ti_3C_2T_x$ MXene synthesized *via* HF etching, illustrating the morphology at different pH values after the washing process. Reproduced from ref. 18 with permission from Elsevier, copyright 2021.

using hydrofluoric acid (HF) as the etchant for the MAX phase. Due to their unique physicochemical properties, MXenes have emerged as promising materials for a wide range of applications, including sensors, lithium-ion batteries, biomedicine, solar cells, electromagnetic interference shielding, gas sensors, and supercapacitors. Since then, extensive investigations have been conducted on MXenes across various fields. Notably, significant progress has been achieved in utilizing MXenes for electrocatalytic technologies.[27–29]

The HF etching technique offers facile access to MXene synthesis at mild reaction temperatures (Fig. 1b). It involves the selective removal of the Al layer from the MAX phase using HF, followed by shaking or sonication, resulting in a nanosheet structure.[30]

The resulting accordion-like morphology necessitates subsequent delamination to obtain monolayer or few-layer MXenes, which typically requires a more sophisticated process. Given the hazardous nature and high toxicity of HF, a safer alternative has been developed through *in situ* HF etching by combining hydrochloric acid (HCl) with lithium fluoride (LiF).[32] In this approach, HCl reacts with LiF to generate *in situ* HF, while the resulting Li^+ ions intercalate between the MXene layers, increasing interlayer spacing and facilitating the formation of monolayer or few-layered MXenes.[33] The presence of F^- ions in the etching solution poses significant environmental risks. In terms of surface functionalization, MXenes

with a high concentration of fluorine groups are detrimental to their energy storage activities. It has been demonstrated that fluorine-free MXenes exhibit superior structural stability and lower environmental hazards compared to conventionally etched MXenes.[34,35] Among the emerging etching strategies, the molten salt method has shown promise in producing desired surface F-free termination groups and scaling up the preparation of MXenes. The synergistic effect of multilayered morphology and the bonding between Ti–C layers significantly influences the electrical properties of MXenes (Fig. 2). Interface scattering can be minimized due to electron transmission between layers, facilitated by the presence of metal d-electrons. Additionally, the surface termination groups (T_x) can modulate electron density and contribute to pseudocapacitive behavior through faradaic reactions, thereby enhancing both electrical conductivity and energy storage capabilities.[36,37]

The properties of MXenes are influenced by both surface termination groups and unsaturated metal sites, which provide active sites and electrostatic charge on the MXene surface. MXenes exhibit excellent mechanical properties, including high strength and flexibility, attributed to the presence of covalent bonds and *van der Waals* interactions.[38] These characteristics enable their application in both rigid and flexible systems, such as wearable electronics and structural reinforcement. Moreover, their broad-spectrum light absorption facilitates applications in

photocatalytic activities through surface plasmon resonance effects.

The electrical properties of MXenes are critical to their functional applications and are significantly influenced by the material type and synthesis methods, which determine their morphology, surface termination groups, and lateral dimensions. Maleski and co-workers reported that the lateral size of MXene nanosheets impacts both optical and electrical properties.[39] Specifically, films fabricated from large-sized MXenes exhibited a peak conductivity of approximately 5.000 S cm^{-1}, compared to around 1.000 S cm^{-1} for those derived from smaller MXene nanosheets. This enhancement is attributed to the more compact stacking of larger flakes, which reduces interlayer gaps and improves charge transport.

Furthermore, MXenes synthesized using traditional HF-based etching methods show higher electrical conductivity than that produced *via in situ* HF generation. In terms of surface chemistry, MXenes with oxygen (O) terminations demonstrate lower electrical conductivity than their hydroxyl (OH)-terminated and unmodified counterparts. Additionally, MXenes treated under an argon atmosphere exhibit reduced conductivity relative to those treated with ammonia. This difference is likely due to the nitridation process in ammonia, which helps preserve the electron-rich structure, thereby enhancing conductivity.[40,41]

3. Properties of Ti$_3$C$_2$T$_x$

MXenes exhibit excellent mechanical properties owing to the robust covalent bonding between the M and C layers. Upon removal of the Al layer, the strength of the M–C bonds is further enhanced due to the high elastic constant, particularly when functionalized with surface termination groups.[42,43] It has been confirmed that nitride-based MXenes possess a higher Young's modulus than carbide-based MXenes, which can be attributed to the higher electronegativity of nitrogen compared to carbon. Surface terminations also significantly influence the strength of M–X bonding. Among the functional groups, O-terminated MXenes demonstrate higher mechanical strength but lower electrical conductivity than OH-terminated counterparts.[44–46] This behavior can be explained by the strong covalent bonds formed between oxygen and the M layer, which reduce the number of free electrons available to facilitate electrical conduction.

The electronic properties of MXenes are strongly influenced by the number of layers, the nature of the energy band gap (direct or indirect), and the type of surface termination groups. Monolayer MXenes typically exhibit larger band gap values compared to their multilayer counterparts, and it is evident that monolayers generally possess an indirect band gap. Surface terminations T$_x$ play a crucial role in determining the metallic or semiconducting behavior of MXenes. While pristine MXene nanostructures exhibit metallic characteristics, they can be transformed into semiconductors through appropriate functionalization.

Density functional theory (DFT) calculations reveal that –OH-terminated and –F-terminated MXenes exhibit band gaps of approximately 0.1 eV and 0.05 eV, respectively.[47] These narrow band gaps ensure high electron mobility, thereby enhancing electrocatalytic performance. Furthermore, substituting Ti with Mo to form Mo$_2$TiC$_2$(OH)$_2$ has been reported to yield an energy band gap as low as ∼0.05 eV.[48]

MXenes exhibit a wide range of optical behaviors, including absorption, refractive index, and reflectivity. Specifically, Ti$_3$C$_2$T$_x$ MXene demonstrates approximately 92% transmittance at wavelengths below 500 nm and about 77% at 550 nm.[42,49] As shown in Fig. 3a and b, the samples exhibit a transmission of approximately 86% in both the visible (VIS) and near-infrared (NIR) regions. The intrinsic absorption of the glass substrate is evident from the dip in transmission below 390 nm. Furthermore, the sheet resistance increases from 400 to 700 Ω sq^{-1} with enhanced transparency, which can be attributed to reduced layer overlap and weaker flake networking at the grain boundaries.[49] This phenomenon suggests that MXene holds great potential for photoelectrochemical and optoelectronic applications. The optical properties of MXene can be effectively tuned by adjusting its thickness, surface functional groups, and intercalated ions. For instance, treatment with tetramethylammonium hydroxide enhances the transmittance from 75% to 92%, whereas urea and hydrazine reduce the transmittance.[46]

One of the major disadvantages of Ti$_3$C$_2$T$_x$ MXene is its susceptibility to oxidation under high-humidity ambient conditions. MXene can be oxidized to form TiO$_2$ in oxygen- and moisture-rich environments.[50] Larger-sized MXene flakes are more resistant to oxidation compared to smaller ones. Furthermore, elevated temperature, high concentrations of storage solvents, and UV illumination can accelerate the oxidation process.[51] It has been demonstrated that MXene can be well dispersed in organic solvents, among which anhydrous isopropanol is more effective in preventing oxidation than water.[52,53]

To mitigate the oxidation of MXene under ambient conditions, antioxidation strategies such as the use of sodium L-ascorbate or polyanions have been employed.[54,55] These treatments effectively preserve the physicochemical properties and the characteristic accordion-like morphology of MXene, allowing it to remain stable for up to three weeks when stored in a sodium L-ascorbate solution.

Based on DFT calculations, pristine MXene exhibits intrinsic magnetic properties, which can be significantly altered upon the introduction of functional groups. The magnetic behavior depends strongly on the type of transition metals and the nature of surface terminations. For instance, Ti$_3$C$_2$ and Ti$_4$C$_3$ are inherently magnetic MXenes, but they become non-magnetic once functional groups are introduced. This phenomenon can be explained by the formation of p–d bonding between the transition metal atoms and T$_x$ groups, as well as orbital splitting effects.[56,57] Specifically, the formation of an octahedral coordination cage around the metal layer leads to splitting of the d orbitals into the t$_2$g (d$_{xy}$, d$_{yz}$, and d$_{xz}$) and eg (d$_{x^2-y^2}$ and d$_{z^2}$) manifolds. Since the t$_2$g orbitals have lower energy than the eg orbitals, the electronic configuration of the d orbitals, and thus the magnetic properties, are modified.[56,58]
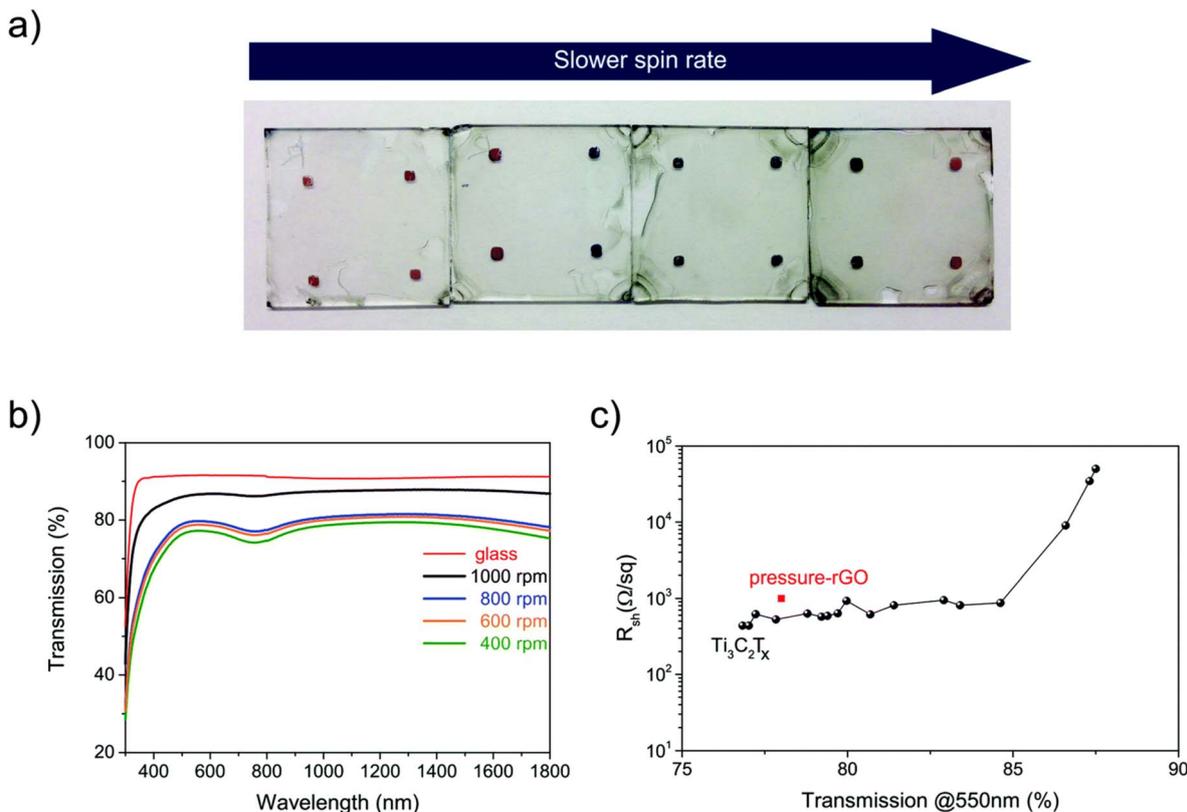
Fig. 3 (a) $Ti_3C_2T_x$ MXene films were deposited on glass slides along with (b and c) their corresponding transmission spectra and sheet resistance. Reproduced from ref. 49.

4. Potential application of $Ti_3C_2T_x$-based electrocatalysts

$Ti_3C_2T_x$ is a typical MXene, accounting for about 70% of related publications in the past decade due to its mechanical flexibility for practical applications and well-established, scalable synthesis from MAX phases. As a 2D layered structure, $Ti_3C_2T_x$ possesses a large effective surface area with tunable interlayer spacing that adjusts binding to intermediates. It exhibits outstanding metallic conductivity (up to 10 000 S cm^{-1}), enabling fast electron transfer. The terminal T_x groups render the surface hydrophilic, ensuring good electrolyte wetting.[59–61] Specifically, during the etching stage, the surface becomes terminated with functional groups such as –O, –OH, and –F, which impart hydrophilicity and increase interlayer spacing, thereby enhancing the accessible area for reactions.[14,62] The termination also plays an important role in boosting the electrocatalytic efficiency of $Ti_3C_2T_x$ based on the tunability of electronic states and active sites, such as direct participation in the reaction or an anchor support for catalyst nanomaterials on the MXene surface.[63–65] However, pristine $Ti_3C_2T_x$ itself exhibits limited intrinsic activity and suboptimal binding energy.[66,67] Recently, there has been a great effort to enhance the performance of $Ti_3C_2T_x$-based electrocatalysts by tuning terminal groups, defect engineering, doping, interlayer engineering or creating heterostructures to anchor the active components and regulate the electronic structure, adjust binding energies and

enhance stability, as illustrated in Fig. 4. Depending on the specific applications, their mechanisms and state of the art will be discussed further.

4.1 Hydrogen evolution reaction

The HER is a fundamental electrochemical process regarding the reduction at the cathode, where protons or water molecules are converted to hydrogen gas (H_2). Hydrogen is known as an eco-friendly fuel due to its only water vapor exhaust, high efficiency and carbon-zero process. Water splitting is a promising method for hydrogen production that aligns with sustainability goals, with the HER serving as a key half-reaction in which protons and hydroxyl ions from water are converted to hydrogen gas. Conventionally, platinum (Pt) is well-known as a near-ideal catalyst for the HER, but Pt is expensive and scarce, posing challenges for wide adaptability. Therefore, there is a critical need to identify cost-effective alternatives to Pt without compromising catalytic efficiency. Superior to other 2D materials, MXenes have gained significant attention due to their excellent electrical conductivity and high surface area from nanolayers, which benefit electrocatalytic performance.[68] However, their performance is generally lower than Pt-based systems due to the limited intrinsic activity and poor adsorption of hydrogen on the surface.[63,68,69]

As shown in Fig. 5a, the hydrogen evolution reaction (HER) proceeds *via* either the Volmer–Tafel or Volmer–Heyrovsky pathway. Starting with the Volmer step, a proton (H^+) in acidic
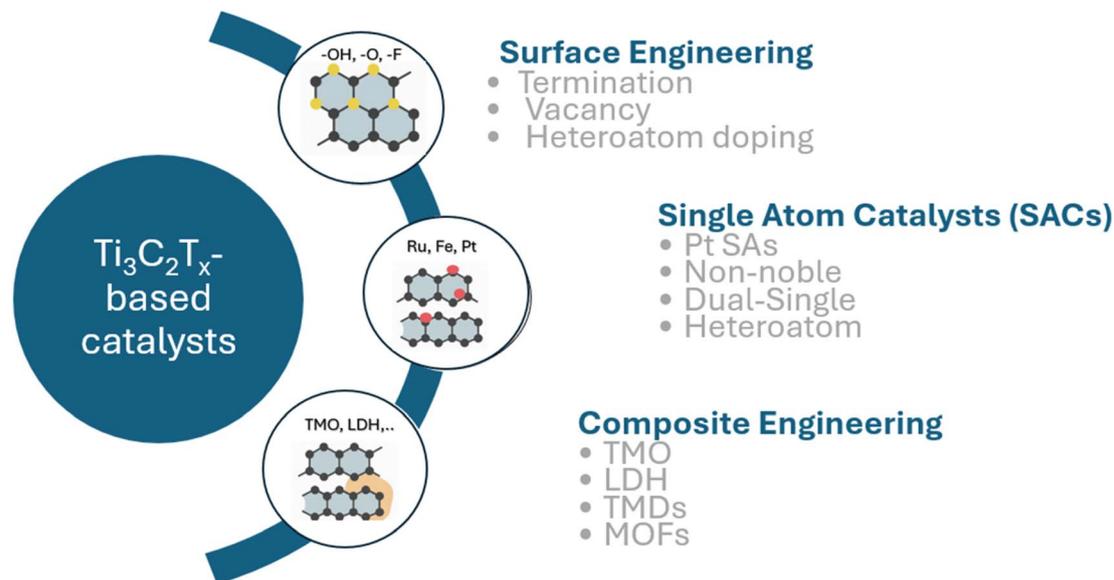
Fig. 4 Overview of various material engineering strategies to improve the electrocatalytic performance of MXene-based systems.

media or a water molecule (H_2O) in an alkaline environment is electrochemically reduced to an adsorbed hydrogen intermediate (H*) on the catalyst surface. Hydrogen gas (H_2) is then formed either by the combination of two H* species in the Tafel step or by the reaction of H* with a proton and an electron in the Heyrovsky step. The Tafel slope can be used to identify the rate-determining step (RDS), the slowest elementary step that controls the overall reaction rate in the HER.[70] Specifically, typical Tafel slopes of about 120, 40 and 30 mV dec^{-1} correspond to the limited kinetics of Volmer, Heyrovsky, and

Tafel steps, respectively. These values provide insight into whether hydrogen adsorption, electrochemical desorption or chemical recombination controls the overall reaction rate. From the thermodynamic perspective, the hydrogen adsorption free energy (ΔG_{H*}) is considered as a key parameter for HER activity. If the values of ΔG_{H*} are too positive, it will hinder proton adsorption, resulting in sluggish Volmer kinetics. Meanwhile if those values are too negative, it will impede hydrogen desorption, reflecting overly strong H* binding in the Tafel or Heyrovsky step. An ideal ΔG_{H*} is near 0 eV, ensuring a balance
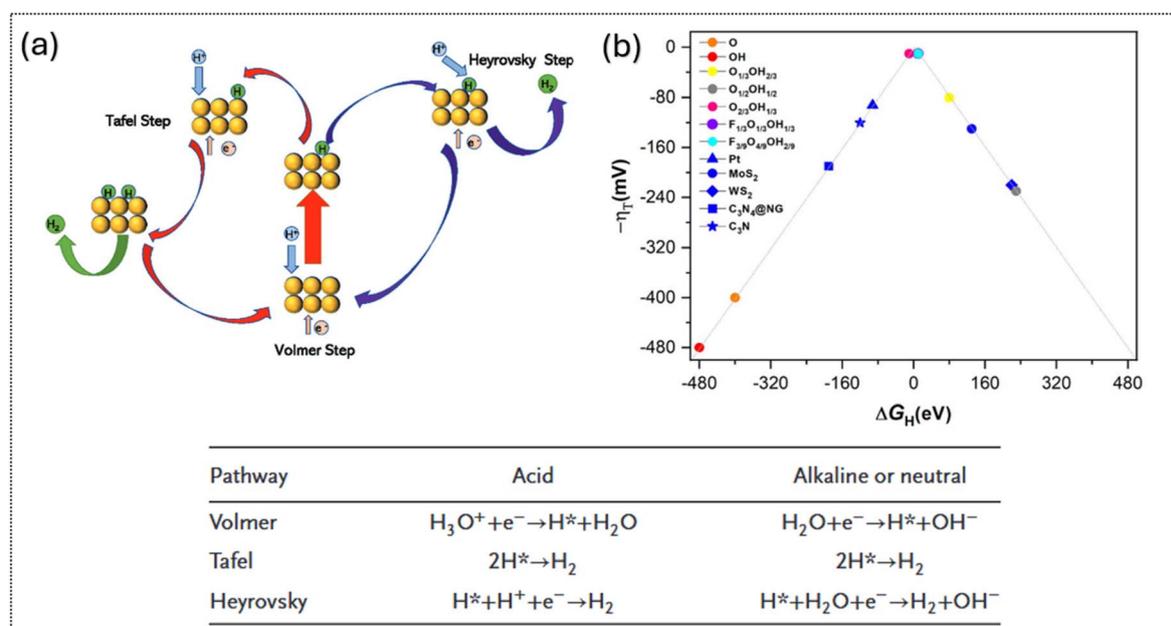

Fig. 5 (a) Schematic of the hydrogen evolution mechanism on the electrocatalyst surface: blue = protons, green = hydrogen intermediates/molecules, yellow = metal atoms; the inset shows HER pathways in different electrolytes with the corresponding reaction steps. Reproduced under the terms of the CC-BY license.[71] Copyright 2023, Wiley-VCH. (b) Volcano plot of theoretical overpotential (η) vs. ΔG_H for differently terminated $Ti_3C_2T_x$ surfaces. Reproduced under the terms of the CC BY-NC license.[72] Copyright 2023, RSC.

between adsorption and desorption for optimal HER performance.[71] This ideal condition is commonly represented by the volcano-type relationship in Fig. 5b, where optimal catalysts lie near the peak and exhibit minimal overpotential. In the same figure, an overview of theoretical studies on MXenes with different surface terminations and other HER catalysts is presented. As indicated by the color-coded regions, functionalized MXenes occupy a more optimal position on the volcano plot relative to conventional HER catalysts. The blue region represents a comparison of different surface terminations, such as –O, –OH, and –F/–OH, demonstrating that surface functionalization is key to enhancing HER activity.

To date, several strategies have been proposed to achieve an optimal ΔG_{H^*} for $Ti_3C_2T_x$-based catalysts. These include surface engineering through tailoring the terminal functional groups or defect introduction to modulate the electronic structure. Increasing the density of active sites enhances the number of sites with near-optimal ΔG_{H^*}, thereby improving reaction kinetics. In addition, forming composites with transition metals or hydroxides promotes water dissociation during the Volmer step under alkaline conditions. The synergistic effect of composites not only increases the catalyst sites but also improves the catalyst stability during long-term operation. When combined, these approaches offer a comprehensive route to maximize HER performance in $Ti_3C_2T_x$-based catalysts.[64,73–76]

One of the early studies related to surface engineering concerns the termination group (T_x). Theoretical calculations of the change in the free energy for H adsorption (ΔG_H) can be used to estimate the HER activity of a catalyst, with an ideal HER catalyst (ΔG_H) value close to zero, where hydrogen adsorption and desorption are balanced, leading to fast Volmer and Tafel/Heyrovsky steps. Specifically, F^- ions are introduced into the titanium carbide MXene during MAX etching; however, fluorine has been shown to inhibit the HER activity of titanium carbide MXene due to unfavorable thermodynamics.[77] In the theoretical study by the Illas team,[72] DFT results to calculate Gibb's energy, combined with Pourbaix and Bader analysis, revealed that the terminations on Ti_3C_2 MXene differently influence hydrogen adsorption and desorption, thereby affecting the HER. For instance, F-termination binds H too weakly, leading to Volmer limitation. They recommended that tuning the ratio of O, OH, and F terminations is key to optimizing catalytic performance.

According to Handoko at el.,[78] increasing F surface coverage on $Ti_3C_2T_x$ leads to a marked decrease in HER activity. Meanwhile, fully O-terminated $Ti_3C_2T_x$ exhibits the most favorable basal-plane coverage at zero applied potential, with a near-zero ΔG_H value comparable to that of Pt.[77] In 2019, Jiang et al.[77] proposed a method to fully functionalize $Ti_3C_2T_x$ with oxygen ($Ti_3C_2O_x$), resulting in enhanced HER performance, with an overpotential (η_{10}) and Tafel slope of 190 mV and 60.7 mV dec^{-1}, respectively, superior to the 266 mV and 109.8 mV dec^{-1} observed for $Ti_3C_2T_x$. It demonstrates that the strategy of surface modification is an effective way for enhancing the catalytic performance of $Ti_3C_2T_x$.

Single-atom catalysts (SACs) consist of mononuclear metal atoms anchored on support layers to maximize atomic efficiency, enabling nearly 100% atomic utilization while minimizing noble or transition metal loading. Beyond cost reduction, the defining advantage of SACs in the HER lies in their well-defined coordination environment and tunable electronic structure, which allow precise regulation of hydrogen adsorption and reaction kinetics at the molecular scale. Currently, in MXene-based SAC systems, various defect engineering strategies, such as metal or carbon vacancies and surface termination vacancies, heteroatom-doped coordination motifs, and strong metal–support interactions (SMSIs), are employed for these composites.

The enhancement of MXene catalysts by SACs can be attributed to synergistic mechanisms. Specifically, defect sites provide localized charge redistribution and unsaturated coordination environments, which generate strong binding energies between the metal atoms and the $Ti_3C_2T_x$ substrate, stabilizing the atoms during electrochemical operation. This improves structural stability and helps maintain catalytic activity under prolonged HER conditions. The isolated metal atoms in SACs function as discrete active centers whose electronic states differ fundamentally from those of nanoparticles or bulk materials. Herein SACs offer a strong electronic coupling between the single atom and the MXene support, inducing charge transfer and d-band modulation of the metal center. That combination helps to adjust the hydrogen adsorption free energy (ΔG_{H^*}) toward the optimal value of approximately 0 eV in the volcano plot. Therefore, SACs can simultaneously facilitate hydrogen adsorption in the Volmer step and hydrogen desorption in the subsequent Heyrovsky or Tafel step, which overcomes kinetic limitations commonly observed in conventional catalysts.

Furthermore, in alkaline HER, where water dissociation is often the rate-determining step, SAC-supported MXenes can exhibit bifunctional reaction sites. The single metal atom preferentially adsorbs hydrogen intermediates (H*), while adjacent Ti–O or Ti–OH species on the MXene surface promote H_2O activation and OH^- desorption. An innovation of N-coordination anchoring also has been proved in SAC synthesis to improve the stability of metal adatoms on C–M–N structure motifs. It is explained by the ability to create multi-point anchoring (M–N and M–C interactions), raise the migration energy barrier for the metal atom and suppress sintering and leaching problems of SACs. As the stability of SACs is affected by the dynamic coordination environment, it is noted that this composite catalyst is only suitable for the HER and not for anodic reactions. In addition, during HER operation, surface terminations can be rearranged, and the Ti surface can undergo partial reconstruction, which may alter metal–support interactions and change the coordination geometry of the SAC over time.

Various synthetic strategies, including wet-chemical impregnation, atomic trapping, and vapor-phase or electro-chemical deposition, have been employed to construct SACs with controlled coordination environments, as illustrated in Fig. 6a. These methods prevent aggregation and stabilize the single atoms through strong interactions such as covalent bonding or metal–support interactions.[63,64]
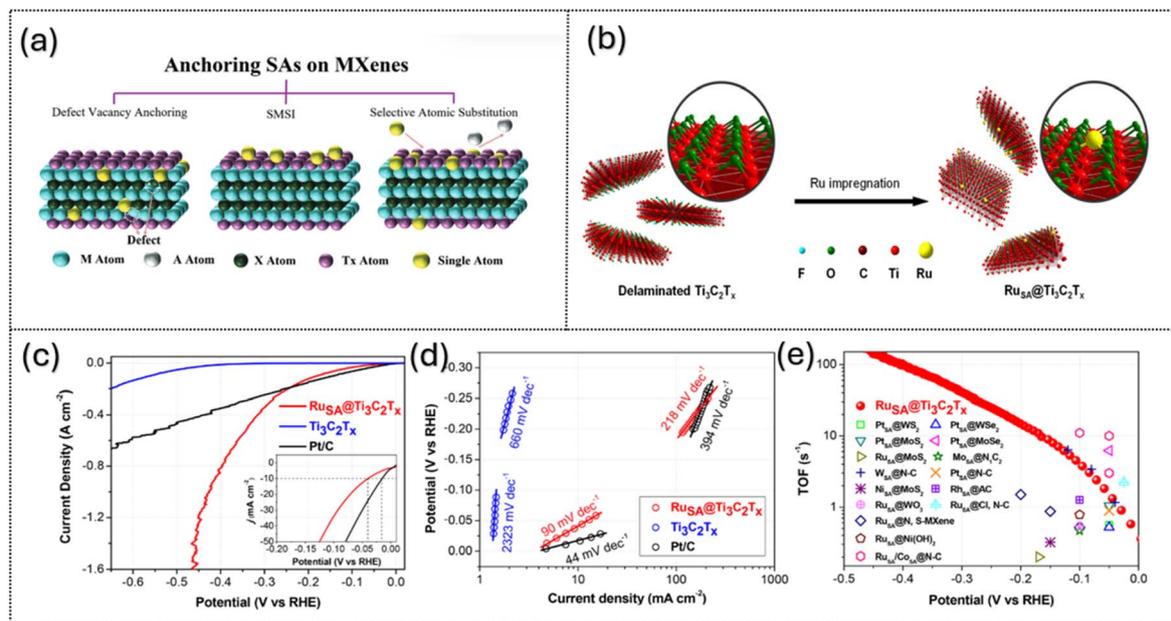
Fig. 6 (a) Illustration of three pathways for anchoring single metal atoms on $Ti_3C_2T_x$-MXene. Reproduced under the terms of the CC-BY license.[63] Copyright 2025, Wiley-VCH. (b–e) Schematic illustration of RuSA@$Ti_3C_2T_x$ synthesis and its hydrogen evolution reaction (HER) performance. Reproduced under the terms of the CC-BY license. Copyright 2023, Wiley.

For instance, RuSA@ $Ti_3C_2T_x$ was fabricated by anchoring Ru single atoms onto $Ti_3C_2T_x$ *via* covalent bonding with surface oxygen (–O) groups, as shown in Fig. 6b, forming Ru–O–Ti bridges, with the Ru atoms uniformly distributed with a content of 0.44 wt%.[79] This structure exhibits significantly enhanced HER performance (Fig. 6c–e), with a Tafel slope of 90 mV dec^{-1}, compared to 44 mV dec^{-1} for the Pt/C reference catalyst. Supported by the $Ti_3C_2T_x$ platform, Ru SAs serve as highly active centers for water splitting, accelerating the Volmer step, with the hydrogen binding energy reduced to 0.07 eV, close to the optimal value for H_2 evolution. Furthermore, the turnover frequencies (TOFs) of RuSA@ $Ti_3C_2T_x$, shown in Fig. 6e, indicate equivalently good performance with other SA-based cathodes. The TOF of RuSA@$Ti_3C_2T_x$ increases exponentially with increasing cathodic potentials, indicating superior catalytic capability at high current densities. This highlights the potential of the $Ti_3C_2T_x$ support in efficiently utilizing quantum effects to improve catalytic performance.[79]

Furthermore, the integration of surface engineering with single-atom composites has emerged as a promising strategy for enhancing HER catalysis. Gong *et al.*[71,80] developed Pt single atoms on $Ti_3C_2T_x$ (0.84 wt%) *via* a thermal shock method that simultaneously generated oxygen vacancies, which are favorable anchoring sites that stabilized Pt atoms and enabled exceptional performance, including a low overpotential of 38 mV at 10 mA cm^{-2}, a Tafel slope of 45 mV dec^{-1}, and a near-optimal Gibbs free energy of 0.02 eV for hydrogen adsorption.

Bifunctional systems of SAs have been explored to enhance electrocatalysts recently regarding $Ti_3C_2T_x$-MXene. Herein, Guo *et al.*[74] proposed a composite of Co/Co_3O_4/$Ti_3C_2T_x$; in this design, $Ti_3C_2T_x$ serves as a stable scaffold offering numerous attachment sites for Co/Co_3O_4 and forms a highly conductive

network that facilitates rapid electron transfer during electrocatalysis. Co_3O_4 has an important role in enhancing hydrophilicity, thereby accelerating bubble release. Meanwhile, the Co/Co_3O_4 phases promote H_2O adsorption and dissociation, boosting H_2 production. As a result, the composite exhibits excellent HER activity and durability in 1 M KOH, achieving an overpotential of 87 mV and a Tafel slope of 61.9 mV dec^{-1} at 10 mA cm^{-2}.

Heteroatom doping with non-metals such as nitrogen, boron, or sulfur can improve MXene catalysts by changing their electronic structure, creating lattice defects, and adding new active sites. In 2023, Kim and co-workers[76] used a one-step hydrothermal process to prepare boron and sulfur co-doped $Ti_3C_2T_x$ (B,S–$Ti_3C_2T_x$) from Ti_3AlC_2, as shown in Fig. 7. B and S co-doping in $Ti_3C_2T_x$ redistributes charge and creates active sites: B–O–Ti and B–O–B sites adjust the electron density of Ti–C to favor H* formation in the Volmer step, while S sites promote proton/electron transfer and stabilize intermediates, accelerating H_2 generation, as shown in Fig. 7a. Characterization revealed that Raman spectra confirmed more defects, and XPS showed electron transfer from Ti to B while DFT calculations indicated lower hydrogen adsorption free energy than that of undoped MXene about 0.087 eV. The catalyst reached an overpotential of 110 mV at 10 mA cm^{-2} with a Tafel slope of ~54 mV dec^{-1}, with the improvements attributed to the combined effects of boron, sulfur, and $Ti_3C_2T_x$ in accelerating HER steps, as shown in Fig. 7b and c. Electrochemical tests showed that the electrochemical double-layer capacitance (C_{dl}) which is often used to estimate the electrochemically active surface area of the catalyst B,S – $Ti_3C_2T_x$ has C_{dl} more than 10 times higher than that of pristine $Ti_3C_2T_x$, indicating that boron and sulfur doping significantly increase the number of
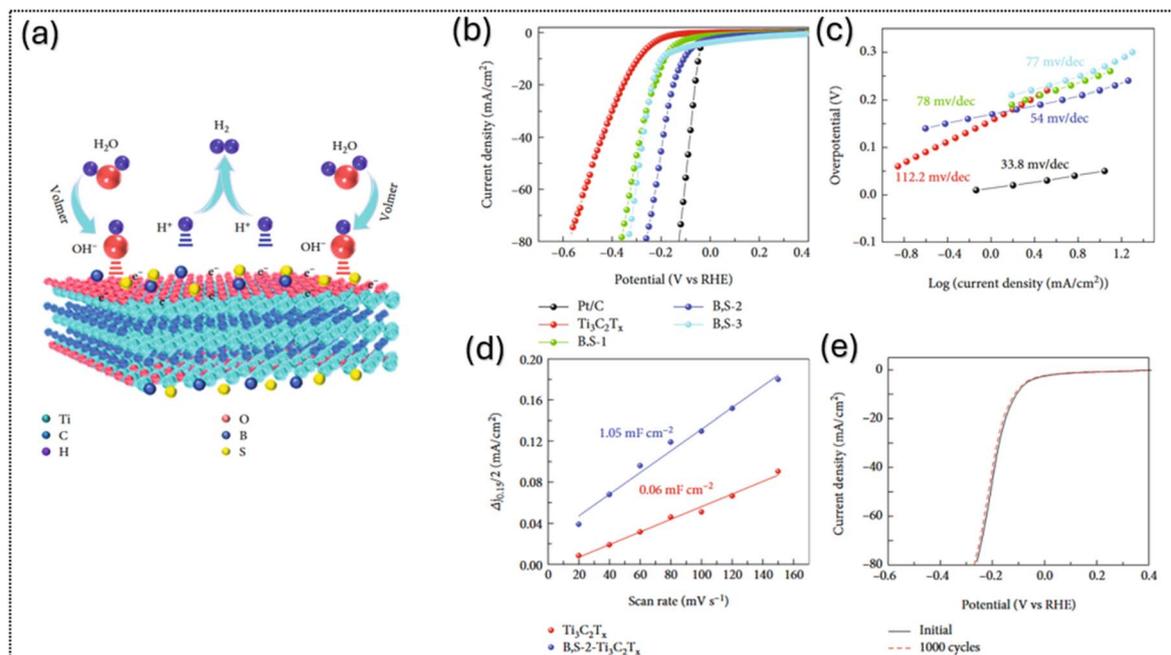
Fig. 7 (a) Graphical illustration of the HER catalysis mechanism for B, S − $Ti_3C_2T_x$ in an acidic medium; electrochemical performances of the as-prepared catalysts in 0.5 M H_2SO_4 with (b) LSV curves, (c)Tafel plot, (d) double-layer capacitance (C_{dl}) at 0.15 V vs. RHE as a function of the scan rate and (e) polarization curves of B, S − $Ti_3C_2T_x$ catalysts before and after 1000 CV cycles (at a scan rate of 50 mV s^{-1}). Reproduced under the terms of the CC-BY license.[76] Copyright 2023, Wiley.

accessible active sites (Fig. 7c); additionally, the sample does not show significant differences before and after cycling, exhibiting excellent HER activity with long-term stability over 1000 cycles (Fig. 7d). This study demonstrates a promising strategy for the metal-free co-doping of MXene nanosheets.

4.2 Oxygen evolution reaction

The OER is the anodic half-reaction coupled with the HER in overall water splitting and in electrochemical processes such as the nitrogen reduction reaction (NRR) and CO_2 reduction reaction (CO_2RR) (Fig. 8a). The OER typically follows the 4e$^-$ pathway involving the adsorbate evolution mechanism (AEM) or lattice oxygen mechanism (LOM). As the reaction happens to be based on the linear scaling relationship between ΔG_{OH}, ΔG_O, and ΔG_{OOH}, and the binding energies of *OH and *OOH are strongly correlated, this imposes a theoretical overpotential limit of 0.37 V when compared with the ideal energy gap of 1.23 V.[60,81]

In the AEM, water or hydroxide is oxidized at active sites (*) through sequential formation of intermediates before releasing O_2 as described in Fig. 8b with *OOH formation as the rate-determining step. As in Fig. 8c, the lattice oxygen mechanism (LOM) eliminates the concerted proton–electron transfer steps as occurred in the conventional AEM, which allows overcoming the AEM scaling limit. Based on direct lattice oxygen participation, such as *O radical formation, lattice–adsorbate O–O coupling, and oxygen vacancy this mechanism does not involve *OOH, so it is positioned as a route to break AEM scaling constraints. In the LOM pathway, the lattice oxygen needs to be active enough to leave or segregate from the lattice and react

with surface oxygen species by generating oxygen via direct O–O bond coupling in highly covalent oxides, where electronic states near the Fermi level have substantial O 2p character, which can be achieved through the defect-engineering route and enhanced metal–oxygen covalency. Although the LOM may lower overpotential and boost intrinsic activity, it can also lead to instability through oxygen vacancy accumulation, metal dissolution, and lattice collapse.[81,82]

Another approach that is introduced to surpass the thermodynamic limitation of AEM overpotential is the oxide pathway mechanism (OPM). In this route, O–O bond formation occurs via direct coupling of two adjacent surface oxo and oxygen-radical species as intermediates, without generating the *OOH intermediate. By removing the *OH–*OOH scaling constraint, this pathway does not require lattice-oxygen participation or an oxygen-vacancy cycle as in the LOM pathway; instead, two surface *O species couple directly to release oxygen. This mechanism is important in water electrolysis because it is targeting the main efficiency bottleneck of energy loss in the OER. However, this pathway requires strict engineering to ensure stable, symmetric adjacent active sites with a narrowly defined inter-site distance to enable a low barrier for oxygen–oxygen coupling, as well as verification by operando characterization for mechanistic validation.

$Ti_3C_2T_x$ MXene is an attractive OER platform due to its metallic conductivity, large surface area, and tunable terminations. However, it requires modification to improve binding with OER intermediates, increase active sites, and enhance stability against oxidation to TiO_2 at anodic potentials.[60] Strategies to improve $Ti_3C_2T_x$ for the OER include electronic
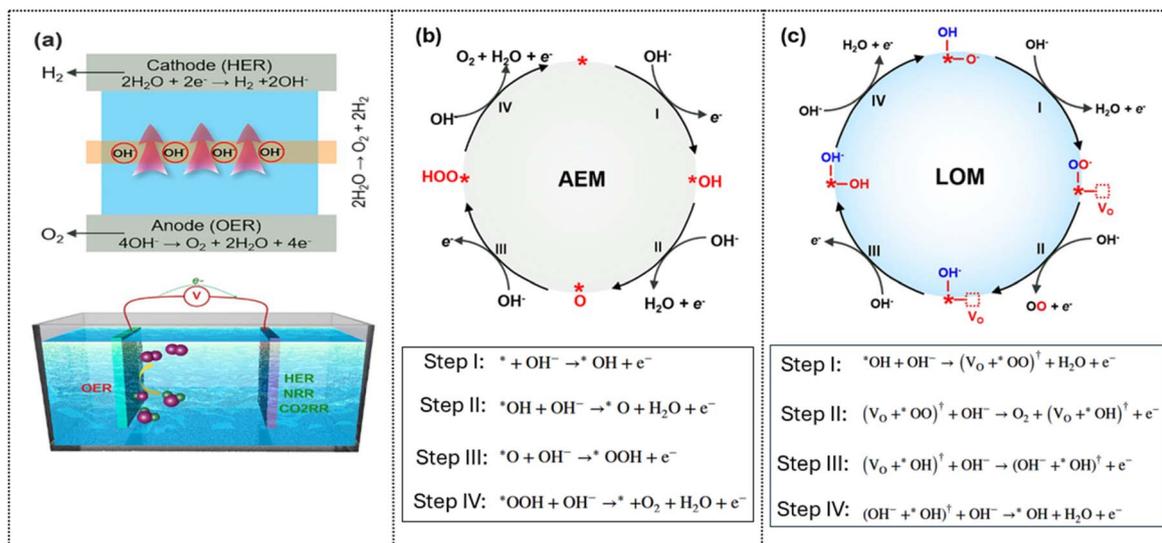
Fig. 8 Illustration of the OER and mechanisms in electrocatalysis: (a) paired with the HER in electrocatalysis; (b) OER catalytic cycle based on the adsorbate evolution mechanism (AEM), and (c) lattice oxygen–mediated mechanism (LOM). Reproduced under the terms of the CC-BY-4.0 license.[81] Copyright 2022, Springer.

structure tuning based on heteroatom doping or defect engineering to optimize adsorption energies toward the volcano plot apex.[60,83] Another approach is to integrate lattice-oxygen-active oxides with $Ti_3C_2T_x$ to form $Ti_3C_2T_x/TiO_2$ heterojunctions, enhancing both activity and conductivity, or to focus on surface oxygen functionalities to increase active oxygen sources and promote proton–electron transfer steps.[60,83]

Heterostructure engineering is a state-of-the-art strategy to optimize $Ti_3C_2T_x$-based OER catalysts by enhancing

conductivity, stability, and activity at the interface. Sheng et al.[84] developed a scalable, in situ guided growth of CoFeLDH while controlling the oxygen ratio on the surface of $Ti_3C_2T_x$ to control the LDH crystal domain size. Fig. 9a displays the procedure to synthesize the composite of CoFeLDH/$Ti_3C_2T_x$ with step 1 tailoring high oxygen (HO MX) or low oxygen (LO MX) and step 2 growing CoFe-LDH with $Ti_3C_2T_x$. O-rich terminations on $Ti_3C_2T_x$ guide LDH nucleation into smaller domains, increasing edge and defect sites for the AEM pathway. Oxygen terminations
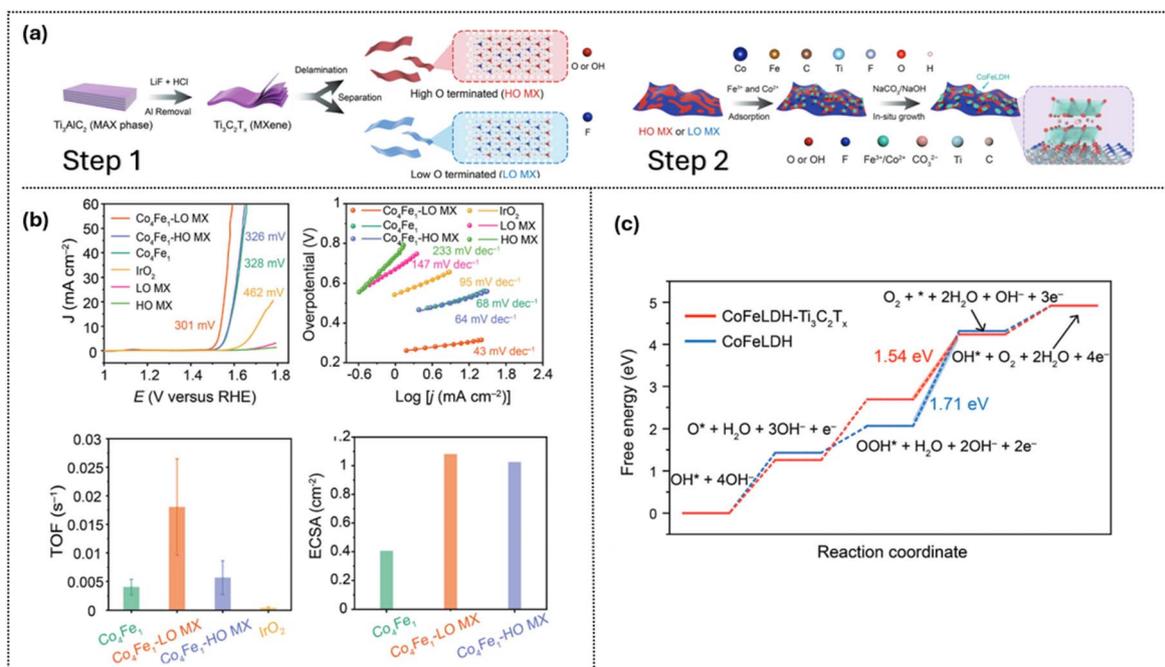
Fig. 9 (a) Schematic of surface termination engineering of CoFe-LDH/$Ti_3C_2T_x$, (b) paired with HER electrocatalysts, (c) electrochemical results from (b), and (d) DFT energy diagram showing reduced energy barriers for OER steps. Reproduced under the terms of the CC-BY license.[84] Copyright 2025, Wiley-VCH.
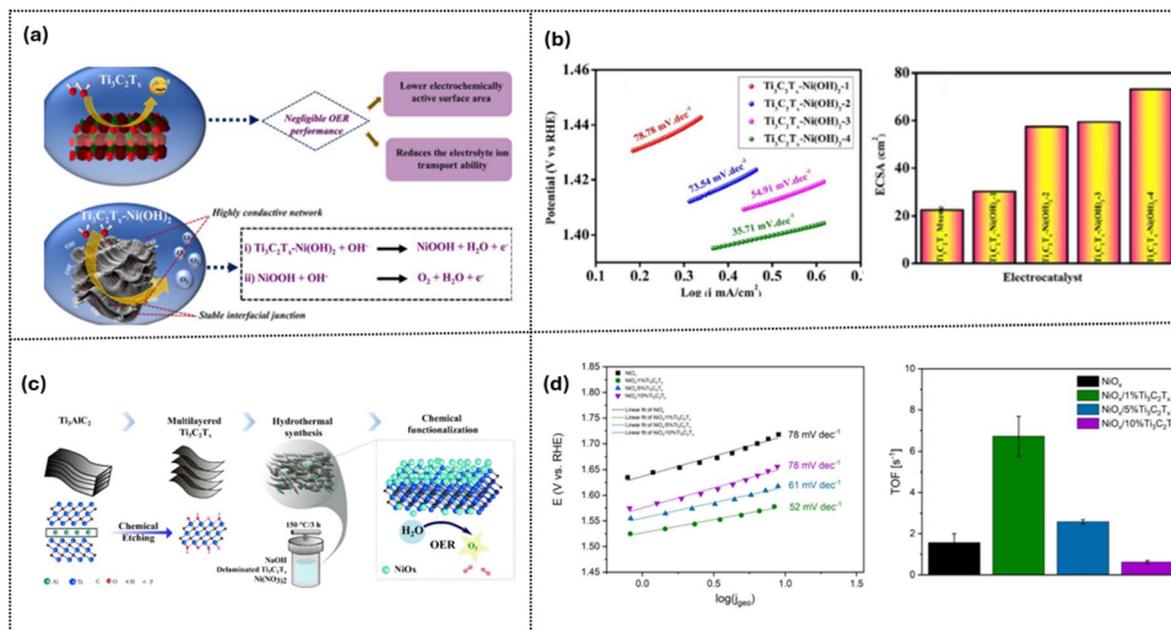
Fig. 10 Ni–$Ti_3C_2T_x$ electrocatalysts for the OER: (a) proposed reaction mechanism, (b) Tafel slopes and ECSA at varying Ni loadings. Reproduced under the terms of the CC-BY license.[86] Copyright 2025, Wiley-VCH. (c) Schematic synthesis route, and (d) Tafel slopes and TOF at varying $Ti_3C_2T_x$ contents. Reproduced under the terms of the CC-BY license.[85] Copyright 2025, Wiley-VCH.

(–O and –OH) on MXene act as anchoring sites; HO MX has a higher density of O terminations, leading to more nucleation points and smaller LDH nanoplates, whereas LO MX has fewer O terminations, which means fewer nucleation sites but stronger interfacial coupling and electronic interaction per nucleation point. As shown in Fig. 9b, CoFe-LDH/LO MX delivers the smallest Tafel slope (43 mV dec^{-1}), the highest turnover frequency (TOF), and the largest electrochemical surface area (ECSA), indicating more efficient active sites and greater accessibility. CoFe-LDH/$Ti_3C_2T_x$ reduces the rate-determining step of the *OOH formation barrier from 1.71 eV (CoFe-LDH) to 1.54 eV via interfacial charge transfer, optimizing intermediate adsorption energies (Fig. 9c). DFT calculations show electron transfer from MXene to γ-CoFeLDH, lowering the rate-limiting barrier through interfacial charge redistribution, domain-size control, and high conductivity, resulting in stable performance in alkaline media and enhanced OER durability in water electrolyzers. The study demonstrates that termination control is a powerful strategy for tailoring nucleation, optimizing interfaces, and enhancing the overall durability of MXene-based OER catalysts.

Transition metal oxides have emerged as promising OER catalysts due to their feasibility in large-scale production, with Ni-based materials having been extensively studied for their enhanced OER activity.[85] This is because coupling $Ni(OH)_2$ or NiO_x with $Ti_3C_2T_x$ forms a conductive and stable interface that enhances electron transport and active site accessibility.[85,86] Browne's team[85] in Germany and Oh's team[86] in Korea independently studied how the Ni/$Ti_3C_2T_x$ ratio affects OER performance (Fig. 10). Bare $Ti_3C_2T_x$ shows negligible activity due to a low ECSA and poor intermediate binding, but coupling it with $Ni(OH)_2$ or NiO_x forms a conductive, stable interface that

improves electron transport and active site accessibility (Fig. 10a). Increasing the $Ni(OH)_2$ loading on $Ti_3C_2T_x$ enhances the ECSA, lowers the Tafel slope (from 78 to 35 mV dec^{-1}), and accelerates the OER kinetics (Fig. 10b). $Ti_3C_2T_x$ also promotes the α → β phase transformation in $Ni(OH)_2$, with β-NiOOH as the active phase, and facilitates faster deprotonation in the AEM pathway. However, the lowest ratio of MXene loading (1 wt%) exhibits the highest TOF by balancing electron transport and Ni site exposure, while excessive loading reduces activity due to site blockage and TiO_2 formation (Fig. 10d). These findings underscore the importance of balancing the Ni-MXene ratio to maximize catalytic performance and ensure long-term stability for efficient OER catalysis.

Bifunctional catalysts capable of promoting both the HER and OER have been researched as a practical route toward overall water splitting for hydrogen production. This approach enables simplified electrolyzer architecture and reduces materials costs based on matched electrode kinetics.

In practice, bifunctional HER-OER catalysts for overall water splitting have attracted great attention for combining the merits of both reactions. A symmetric design operating in the same electrolyte simplifies the system, reduces energy consumption and cost, and enables scalable applications. An ideal bifunctional system requires high activity and stability in the same pH environment for both the HER and OER, along with balanced binding energies for hydrogen- and oxygen-containing intermediates. The main challenge is to minimize overpotentials at both electrodes while meeting the optimal surface chemistry requirements of both reactions and maintaining stability at highly reducing and oxidizing potentials in the same electrolyte.[87,88] Regarding this challenge, $Ti_3C_2T_x$ is integrated as a platform to address multiple bottlenecks, including
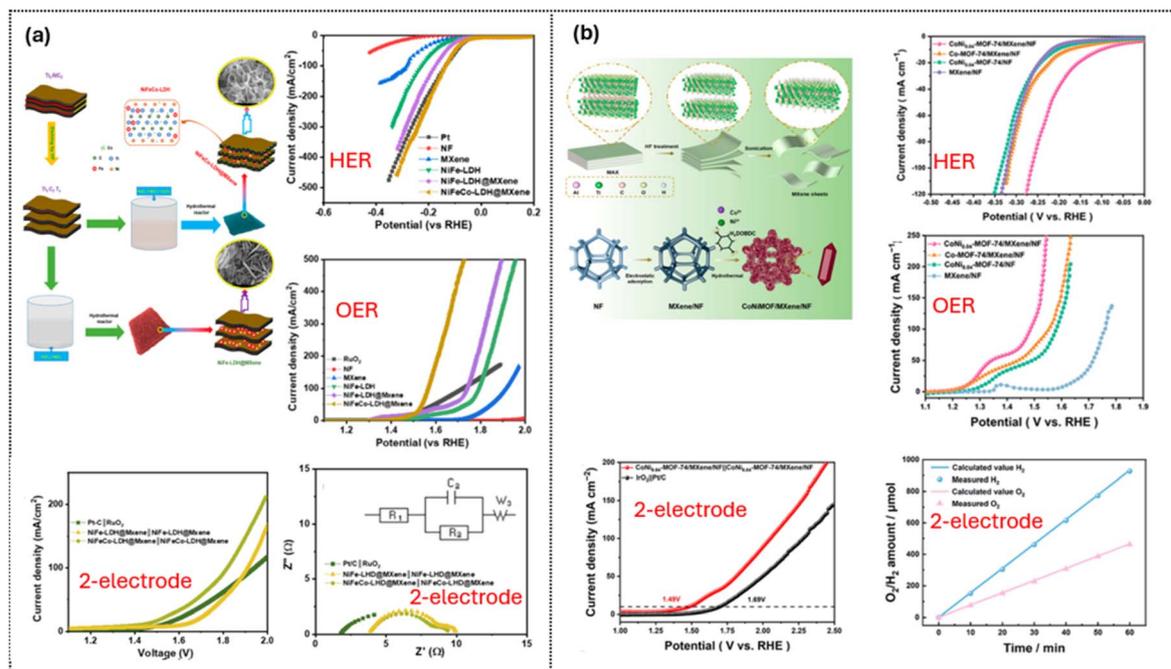
Fig. 11 $Ti_3C_2T_x$–based composites for efficient overall water splitting: (a) synthesis illustration and the electrocatalytic performances of $Ti_3C_2T_x$-supported NiFeCo-LDH. Reproduced under the terms of the CC BY 4.0 license.[91] Copyright 2022, MDPI. (b) Synthesis illustration and the electrocatalytic performances of the Ni-doped Co-MOF-74/$Ti_3C_2T_x$ MXene composite and its electrocatalytic performance. Reproduced under CC BY 4.0.[92] Copyright 2024, MDPI.

improving carrier pathways to accelerate the HER and OER kinetics, tuning surface terminations to adjust adsorption energy, and hybridizing with active phases to achieve optimal binding energies. Its 2D structure can anchor nanoparticles, single atoms, or molecular catalysts, preventing aggregation and enhancing stability under redox cycling.[70,89,90]

An example of prominent studies in this direction is the three-dimensional honeycomb-like structure of NiFeCo-LDH on $Ti_3C_2T_x$ reported by Hussain *et al.*[91] Fig. 11a illustrates the synthesis and electrocatalytic performance of NiFeCo–LDH@$Ti_3C_2T_x$ MXene on Ni foam. The $Ti_3C_2T_x$ scaffold prevents LDH aggregation, exposes more active sites, and maintains open interlayer channels for ion diffusion, forming a honeycomb-like porous structure. Direct growth of NiFeCo–LDH on MXene yields a conductive, hydrophilic electrode with strong interfacial coupling that enhances charge transfer. In the HER, the composite achieves a low overpotential of 34 mV, outperforming all controls. In the OER, it reaches 130 mV with a Tafel slope of 52 mV dec^{-1} and a steeper LSV rise than MXene or NiFe-LDH alone. In overall water splitting, the symmetric NiFeCo-LDH@MXene‖NiFeCo-LDH@MXene cell delivers 10 mA cm^{-2} at 1.41 V, lower than that in Pt/C‖RuO_2 (1.75 V). EIS shows that a smaller semicircle corresponds to faster electron transfer and lower charge-transfer resistance, with NiFeCo-LDH@MXene exhibiting the lowest R_{ct} of 4.6 Ω, confirming superior kinetics and outstanding stability during 24 h of testing. This underscores the synergistic effect of $Ti_3C_2T_x$ in enhancing electron transport, optimizing intermediate adsorption, and stabilizing the structure under redox conditions.

Another innovation was reported by Yu *et al.*[92] with the design of a composite electrode combining nickel foam (NF), $Ti_3C_2T_x$ MXene, and a Ni/Co-based MOF. The resulting CoNi-MOF-74/MXene/NF acts as a bifunctional and durable water-splitting electrocatalyst. As shown in the LSV curves, the composite significantly outperforms Co-MOF-74/NF and MXene/NF controls: for the HER, it achieves an overpotential of 102 mV at 10 mA cm^{-2} with a Tafel slope of 123.5 mV dec^{-1}, consistent with a Volmer-limited mechanism; for the OER, it reaches 100 mA cm^{-2} at 256 mV with a Tafel slope of 40.21 mV dec^{-1}, reflecting fast oxygen evolution kinetics. In a two-electrode configuration using the same material at both electrodes, the system delivers 10 mA cm^{-2} at 1.49 V and operates stably for 40 h with a faradaic efficiency of 97% ($H_2 : O_2 \approx 2 : 1$). Mechanistic studies indicate that Ni doping increases the Co^{3+}/Co^{2+} ratio, generating more active sites, while strong MXene–MOF interfacial coupling lowers charge-transfer resistance and increases double-layer capacitance. After the OER, the catalyst surface partially converts to Co(Ni)OOH, which further optimizes adsorption of *H and O-intermediates and accelerates charge transfer. In both systems, $Ti_3C_2T_x$ acts as a conductive, wettable scaffold that prevents restacking/aggregation, exposes more edge sites, eases Volmer water activation (HER) and OOH formation pathways (OER), and manages gas release, making the composites clearly outperform their individual precursors under practical alkaline conditions.

$Ti_3C_2T_x$ MXene has emerged as an effective platform for seawater electrolysis by mitigating the competing chlorine evolution reaction (CER) and stabilizing catalysts in chloride-rich environments, which is not ideal for the HER/OER as it

Table 1 Summary of $Ti_3C_2T_x$-based catalysts for HER, OER, and overall water–splitting applications

$Ti_3C_2T_x$ composites	Electrolyte	Overpotential [mV]	Tafel slope [mV dec^{-1}]	Application	Ref.
Pristine $Ti_3C_2T_x$	0.5 M H_2SO_4	300	86.6	HER	76
Pristine $Ti_3C_2T_x$	1 M KOH	541	324.46	HER	74
PtSA-$Ti_3C_2T_x$	0.5 M H_2SO_4	38	45	HER	80
RuSA-$Ti_3C_2T_x$	1 M KOH	40.3	90	HER	79
Co/Co_3O_4–$Ti_3C_2T_x$	1 M KOH	87	61.9	HER	74
B, S–$Ti_3C_2T_x$	0.5 M H_2SO_4	110	54	HER	76
CoP–$Ti_3C_2T_x$	0.5 M H_2SO_4	135	48	HER	73
Fe@$Ti_3C_2T_x$	1 M KOH	81	33.03	HER	75
Pristine $Ti_3C_2T_x$	1 M KOH	520	68	OER	91
$Ni(OH)_2$–$Ti_3C_2T_x$	1 M KOH	235.54	35.71	OER	86
CoP@C – $Ti_3C_2T_x$	1 M KOH	235	54	OER	97
Ni–$Ti_3C_2T_x$	1 M NaOH	354	54	OER	85
CoFeLDH-$Ti_3C_2T_x$	1 M KOH	301	43	OER	84
CuS@$Ti_3C_2T_x$	1 M KOH	89.7	54	HER	98
		171	39.3	OER	
NiFeCo–LDH@ $Ti_3C_2T_x$	1 M KOH	34	62	HER	91
		130	52	OER	
$CoSe_2$–$Ti_3C_2T_x$	1 M KOH	230	65	HER	70
		270	71	OER	
CoNi-MOF-74/$Ti_3C_2T_x$/NF	1 M KOH	102	123.5	HER	92
		256	40.2	OER	

competes with the OER, and chloride ions corrode active sites by adsorbing on polarized electrodes. The high conductivity of $Ti_3C_2T_x$ lowers the OER overpotential, making the OER kinetically favorable over the CER, while its tunable surface terminations preferentially stabilize oxygen intermediates rather than chloride ions. In addition, its 2D layered framework provides abundant ion channels and anchors transition-metal nanoparticles or single atoms, preventing aggregation and shielding active sites from chloride attack.[93,94] For example, leveraging the intrinsic properties of NiFe-LDH to repel chloride ions during seawater oxidation,[95] and when integrated with $Ti_3C_2T_x$, the strong Ti–O–Fe bonding, electron withdrawal, and surface charge synergistically suppress corrosion and Cl$^-$ attack while enhancing the lattice-oxygen-driven OER, enabling highly efficient and durable seawater electrolysis.[96]

Table 1 overviews the latest innovations for the HER, OER, and water splitting, with ideas summarized by focusing on non-noble metal alternatives, maximizing the efficiency of quantum catalysts from SA structures, structure engineering through doping, heterostructures, surface modifications, and combining these strategies with excellent performance data. The overall goal is to achieve the lowest overpotential and Tafel slope, which indicate highly active catalytic sites, while also retaining structural stability for long-term use and keeping the approach open for scalable applications.

4.3 Gas conversion reactions

Recently, there have been calls for reducing greenhouse gas emissions to tackle the global climate change. And the innovation of gas conversion to value products such as chemicals or fuels is emerging as a hot topic in the catalyst field. Electrocatalytic gas reduction enables the direct conversion of molecules such as CO_2 (CO2RR), NH_3 (NRR), and O_2 (ORR) to value-adding products as chemicals or fuels. However, conventional catalysts often suffer from low selectivity, slow kinetics, poor stability, harsh operating conditions and reliance on expensive noble metals.[99–103] To address these limitations, $Ti_3C_2T_x$ has emerged as a promising candidate, enabling adsorbate pathways where rates and selectivity are controlled by surface terminations, anchored active sites, and coverage effects that link co-adsorbates to otherwise unfavorable intermediates.[104]

A major focus in gas reduction is the CO_2 reduction reaction (CO2RR), which converts CO_2 into value-added C_1 and C_2^+ products such as methanol, ethanol, ethylene, and acetone. This process faces two key challenges: the insufficient adsorption and activation of intermediates on many electrodes, and strong competition from the hydrogen evolution reaction. On $Ti_3C_2T_x$ MXene, the CO2RR proceeds through proton-coupled electron transfer (PCET) steps involving complex intermediates that depend on the electrocatalyst and reaction conditions. Intermediates formed during the CO2RR through proton–electron transfer steps yield C_1 products (e.g., CO, CH_4, CH_3OH, and HCOOH), while further C–C coupling of CO species leads to C_2 products (e.g., C_2H_4, CH_3CH_2OH, and CH_3COOH).[105] In this context, a DFT modeling study by Lozano-Reis and Exner[106] emphasized the critical role of less-stable intermediates and co-adsorbates in determining CO2RR selectivity on $Ti_3C_2T_x$, particularly through tunable surface terminations. The active Ti sites facilitate CO_2 adsorption, initially forming carbonate-like intermediates where monodentate binding is less stable than bidentate, thereby directing distinct reduction pathways as shown in Fig. 12.

Importantly, adsorption strength must strike a balance: CO_2 should bind strongly enough for activation but not so strongly as to cause surface poisoning, while desired products such as CH_4 require sufficiently weak binding to ensure efficient release and avoid catalyst deactivation. The adsorption-energy trends in
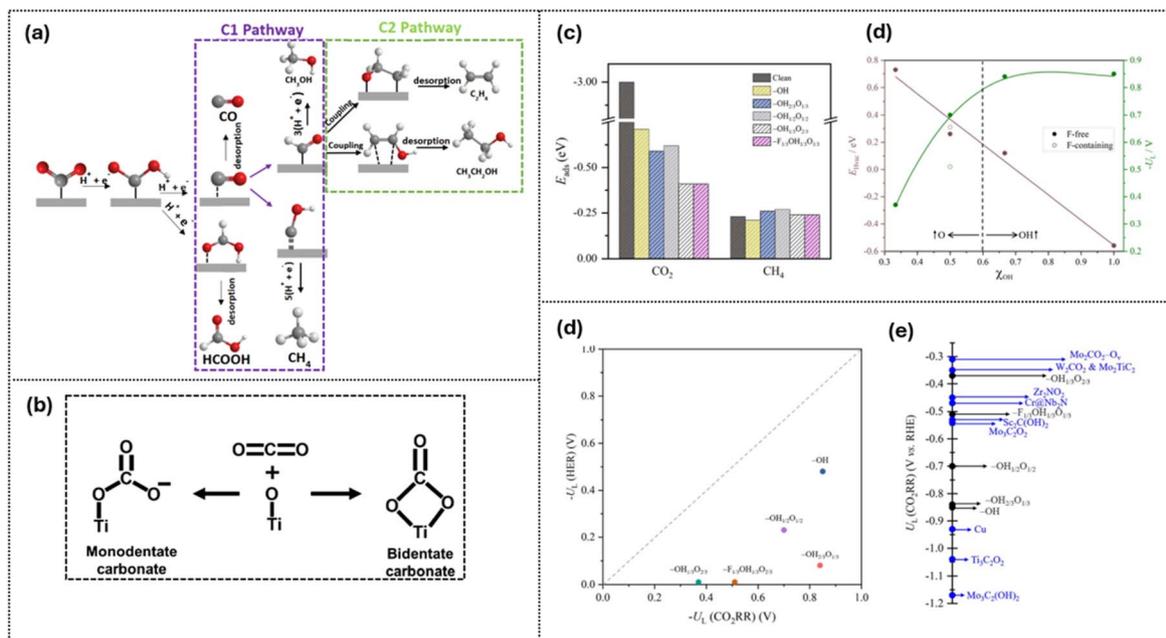
Fig. 12 The illustration of the theoretical model and calculations regarding $Ti_3C_2T_x$ for the CO_2RR: (a) C_1 vs. C_2 pathways for CO_2 electro-reduction. Reproduced under the terms of the CC-BY license.[105] Copyright 2023, MDPI. (b) Proposed CO_2 adsorption geometry on the MXene surface. Reproduced under the terms of the CC-BY license[102] Copyright 2023, RSC. (c) CO_2 and CH_4 adsorption energies corresponding to various terminations of $Ti_3C_2T_x$, (c) H-vacancy energies and limiting potential in terms of oxygen groups of F-controlling $Ti_3C_2T_x$, (d) comparision of limiting potential (UL) of the HER and CO_2RR, (e) comparison of UL of methane from $Ti_3C_2T_x$ with other candidates. Reproduced under the terms of the CC-BY-NC license.[106] Copyright 2024, RSC.

Fig. 12c show that CH_4 binding is already suitable, but CO_2 adsorption on clean $Ti_3C_2T_x$ is too strong. Introducing mixed –O/–OH/–F terminations moderates CO_2 binding into a more favorable activation regime.[106] Termination-controlled thermodynamics further influence the required driving force, as shown in Fig. 12d, with the computed limiting potential (UL) varying with the –OH fraction (χ_{OH}). The results indicate that a balanced presence of –OH and –O groups, with a small proportion of F, optimizes both the limiting potential and proton transfer rate.[106] Consistently, Exner et al.[104] reported that the highest selectivity is observed for CH_3OH and CH_4 at low to medium F coverage, with CH_4 dominating at higher F levels. Since the HER is a key competing pathway, Fig. 12d also displays the comparison of UL(CO_2RR) with UL(HER), identifying termination windows where the CO_2RR is thermodynamically favored. This demonstrates how mixed terminations provide a practical lever for selectivity control. Relative to other catalyst families, $Ti_3C_2T_x$ with optimized O/OH terminations achieves competitive CO_2RR limiting potentials, comparable in magnitude to established Cu- and Mo-based systems, while maintaining the unique advantage of tunable surface chemistry on a highly conductive 2D scaffold (Fig. 12e). This demonstrates that $Ti_3C_2T_x$ is not only tunable but also potentially performs comparably to state-of-the-art CO_2RR catalysts.

Krishnan et al.[102] demonstrated that $Ti_3C_2T_x$ nanosheets enhance CO_2RR performance by offering a highly conductive 2D scaffold with abundant surface terminations that promote CO_2 adsorption and activation. The nanosheets displayed strong CO_2 affinity (0.16 mmol g^{-1} uptake at 298 K) and high

electrochemical activity, evidenced by a large double-layer capacitance (C_{dl} = 3.19 mF cm^{-2}), which correlates with more active sites. During electrolysis, the catalyst achieved a peak faradaic efficiency of 53.8% for liquid products and an overall efficiency of 96%, producing both C_1 (CO and CH_3OH) and C_2^+ products (C_2H_5OH and CH_3COCH_3) at -1.1 V vs. Ag/AgCl in 0.5 M $KHCO_3$ before decreasing due to HER dominance. Stability testing over 72 h at 1.1 V confirmed negligible decay in current density and minimal structural degradation. Although $Ti_3C_2T_x$ MXene exhibits excellent CO_2 adsorption and stability, its limited selectivity, competition with the hydrogen evolution reaction, and complex surface termination structure underscore the need for refined design strategies to enhance its efficiency for CO_2 electroreduction.

Recent advances position $Ti_3C_2T_x$-based MXenes as versatile platforms for the CO_2RR, with composites like oxides, COF hybrids, and single-atom decorations enhancing activity, selectivity, and rates.[107] Formate, a valuable CO_2RR product due to its energy content, can be efficiently produced using $Ti_3C_2T_x$-based catalysts. Notably, SnO_2 quantum dot decoration on $Ti_3C_2T_x$ enables highly selective formate generation, achieving approximately 94% faradaic efficiency and a partial current density of 57.8 mA cm^{-2}. This performance is attributed to reduced interfacial charge-transfer resistance and dynamic modulation of the Sn oxidation state under applied potential, as revealed by in situ synchrotron-based X-ray absorption spectroscopy (XAS).[108]

The development of a 3D Cu–Pd/$Ti_3C_2T_x$ aerogel highlights the role of MXene in enhancing CO_2 adsorption and expanding
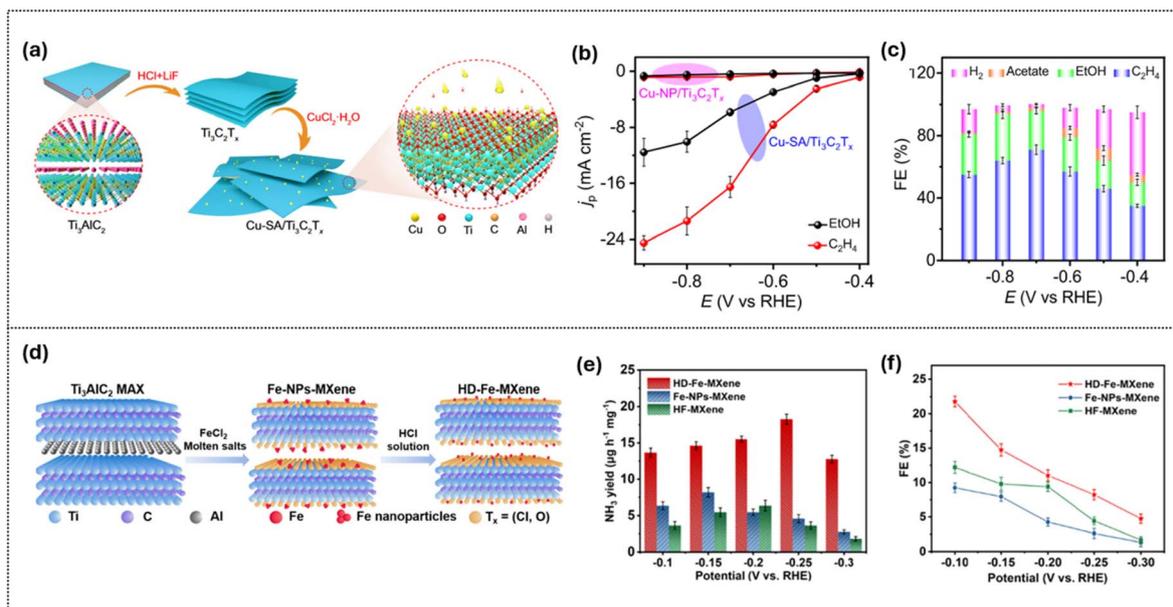
Fig. 13 Synthesis and electrocatalytic performance of single-atom MXene catalysts for CORR and NRR applications. (a) Schematic preparation of Cu single-atom sites anchored on $Ti_3C_2T_x$ and (b) corresponding partial current densities for C_2H_4 and EtOH production. (c) Faradaic efficiencies of H_2 and CO_2 reduction products on Cu-SA/$Ti_3C_2T_x$ at different potentials. Reproduced under the terms of the CC BY 4.0 license.[100] Copyright 2021, Nature Communications. (d) Controlled etching strategy to immobilize Fe atoms in MXene, forming HD-Fe-MXene, and (e) NH_3 yields and (f) faradaic efficiencies at different potentials. Reproduced under the terms of the CC-BY license.[111] Copyright 2022, Wiley.

the electrochemically active surface area within a binder-free, porous architecture that integrates Cu–Pd bimetallic sites. $Ti_3C_2T_x$ supports tuning of active sites and shifts selectivity from CO to formate by providing a lower-energy pathway for $HCOO^-$ formation. Experimental results further show improved charge transfer, facilitated kinetics of the rate-determining step, and mitigation of the limitations of Cu–Pd alone. Consequently, the catalyst achieves an industrially relevant current density of 150 mA cm^{-2} with >90% FE for formate in a membrane electrode assembly, delivering ∼47% full-cell energy efficiency and stable operation for 5 hours.[109]

In a study from Zhao et al.,[110] single-atom Cu anchored on $Ti_3C_2Cl_x$ MXene acts as an effective support, where Cu–O bonding and Cl termination create a distinct pathway toward alcohols. XAS and DFT confirmed that the unsaturated electronic structure of Cu centers lowers the energy barrier for HCOOH* to CHO* conversion, enabling 59.1% FE for methanol in an H-cell with commendable electrocatalytic stability.

In the trend of gas-phase electrocatalysis, studying the CO reduction reaction (CORR) is an effective strategy instead of the CO_2RR, when targeting the crucial C–C coupling stage of the CO_2RR by bypassing the rate-limiting $CO_2 \rightarrow CO$ step and avoiding competing H_2 or HCOOH pathways. Bao et al.[100] demonstrated that anchoring Cu SAs onto $Ti_3C_2T_x$ as isolated Cu–O_3 single sites enables highly efficient C_2^+ production, including ∼71% faradaic efficiency (FE) for ethylene and ∼25% for ethanol, retaining stability for 68 h. As shown in Fig. 13a, the catalyst is synthesized by exfoliating Ti_3AlC_2 into $Ti_3C_2T_x$ and anchoring single Cu atoms, forming well-defined atomic Cu–O_3 sites. This design yields outstanding results. Correspondingly, Fig. 13b shows that partial current densities for C_2H_4 (−16.5 mA cm^{-2}) and EtOH (−5.8 mA cm^{-2}) on Cu–SA/$Ti_3C_2T_x$ far exceed those of Cu nanoparticles, highlighting the role of atomically dispersed sites in accelerating C–C coupling. Finally, Fig. 13c confirms the product distribution across applied potentials, with C_2H_4 dominating, EtOH as the major liquid product, and

Table 2 Summary of $Ti_3C_2T_x$-based catalysts for gas reduction reactions

$Ti_3C_2T_x$ composite/system	Reaction	Best metric (FE or rate)	Main products/selectivity	Ref.
$Ti_3C_2T_x$	CO_2RR	FE: 96%	CO 42.2%, CH_3OH 23.6%, EtOH 20.1%, acetone 10.1%	102
CoPc/o–N–MXene	CO_2RR	FE: 39.5%	CH_3OH	113
Cu single atoms on $Ti_3C_2T_x$	CORR	FE: 71%	C_2H_4	100
Cu–Pd 3D Aerogels/$Ti_3C_2T_x$	CO_2RR	FE: 79%	Formate	109
HD-Fe-MXene	N_2RR $\rightarrow$ NH_3	FE: 21.8%	NH_3	111
$Ti_3C_2T_x$	NO_3RR $\rightarrow$ NH_3	FE: 5.78%	NH_3	114
FeN_4/$Ti_3C_2T_x$	ORR (alkaline)	N/A	H_2O (4e$^-$)	112
(FePc/$Ti_3C_2T_x$)			H_2O_2 < 1%	

the HER strongly suppressed. DFT calculations attribute this performance to the stabilization of the *CO–CHO intermediate at Cu–O_3 sites, lowering the energy barrier for C–C coupling and explaining the high activity and durability relative to nanoparticle counterparts.

For nitrogen chemistry, $Ti_3C_2T_x$ enables efficient N_2 activation when active sites and terminations are co-optimized. Embedding highly dispersed Fe in fluorine-free $Ti_3C_2T_x$ *via* MAX-replacement plus HCl etching yields FE(NH_3) = 21.8% at −0.10 V and an NH_3 yield of 18.25 μg h^{-1} mg^{-1} at −0.25 V in 0.1 M Na_2SO_4 with 24 h/multicycle stability, evidencing that F-removal exposes/immobilizes Fe while curbing the HER. Extending to nitrate reduction, a cross-MXene study finds that Ti_3-based members (including $Ti_3C_2T_x$) lead their class in FE, yield, and stability, with DFT tracing performance to central-metal identity and T_x-controlled adsorption energetics. Together these results define the state of the art: termination/coverage engineering plus site design (dispersed metals or molecular centers) on conductive $Ti_3C_2T_x$ provides coherent levers to tune activity, selectivity, and durability across CO_2RR and N-reduction pathways.[111]

The oxygen reduction reaction (ORR) is a gas-involving electrochemical reaction and is considered the thermodynamic reverse of the OER. In the electrocatalysis field, the ORR governs cathodic performance in fuel cells and metal–air batteries. The ORR involves O–O bond breaking, dominated by adsorption energetics at isolated surface sites. The adsorption-controlled mechanism involves surface-bound oxygen intermediates (*O_2, *OOH, *O, and *OH) with O_2 being sequentially reduced and protonated until the O–O bond is completely cleaved into water or hydroxyl molecules. As the reactions are governed by the adsorption energy of these intermediates, especially *OOH, this results in constraints on strong scaling relationships. However, lattice oxygen participation or oxygen-vacancy dynamics, which can be employed in the OER, does not play a role in the ORR, making breaking of scaling relations much harder in the ORR.[112]

MXenes with the synergetic effects based on metal-like conductivity, tunable surface terminations, and strong interaction with active species have been proposed as a potential candidate for ORR applications with the ability to act as conductive supports, electronic modulators, or anchoring substrates for catalytically active centers. Specifically, oxygen-containing terminations such as –O and –OH can enhance O_2 and *OOH stabilization, shifting the free-energy profile closer to optimal values as predicted by adsorption volcano relationships. MXenes serve as effective supports for SACs and heteroatom-doped motifs for preventing metal aggregation and tuning the d-band center, which can improve the ORR performance. In other words, the electronic environment of the active site is optimized by the MXene substrate.[112]

The state of the art now points toward rational control of termination chemistry, atomic dispersion, and device-level architectures to bridge lab-scale activity with practical gas electroreduction, while open questions remain regarding long-term durability, synthesis scalability, and controlling selectivity

for specific desirable products. More ideas on $Ti_3C_2T_x$-based electrocatalysts for gas reduction are summarized in Table 2.

5. Conclusions and future perspectives

$Ti_3C_2T_x$ MXene has been emerging over the last 5 years, with most results still in theoretical studies. This MXene attracts attention as a promising platform for electrocatalysis thanks to its metallic conductivity, 2D layered structure, and tunable surface terminations. The surface terminations, such as –O, –OH, and –F functional groups, strongly affect catalytic behavior by shaping adsorption energies and the electronic environment of active sites. For instance, –F groups are usually unfavorable for the HER because they hinder proton adsorption, but in the CO_2RR they help suppress hydrogen evolution and stabilize intermediates, indirectly improving selectivity. Beyond its intrinsic activity, $Ti_3C_2T_x$ is also valued as a conductive scaffold with a large surface area that supports charge-carrier transport and adsorption capacity, which is especially useful in gas reduction as it allows more space for gas bubbles during the reaction. It is capable of hosting catalytic centers through strategies such as defect engineering, heteroatom doping, single-atom anchoring, and heterostructure assembly. $Ti_3C_2T_x$ is versatile, with different methods to develop composites and anchor single atoms from both vacancies and terminations. Such approaches have enabled notable advances, from atomically dispersed noble metals to the exploration of new catalysts based on non-noble transition metals or synergistic dual-metal systems, which allow the development of bifunctional HER and OER activity.

As the research field of $Ti_3C_2T_x$ electrocatalysts is still in an early developmental phase, the potential for practical application is evident but remains constrained in practical studies. $Ti_3C_2T_x$ catalysts often require higher overpotentials than noble metals, suffer from oxidation and restacking under harsh conditions, and lack precise control over surface terminations due to current etching methods. Scalability and long-term durability at industrial current densities also remain open questions, with many designs still at the theoretical or proof-of-concept stage. A persistent challenge lies in controlling surface terminations, as conventional etching routes often produce heterogeneous functional groups, leading to variability in catalytic behavior. $Ti_3C_2T_x$ itself possesses limited intrinsic activity; thus, advancing MXene-based electrocatalysts requires strategies to increase active sites, such as vacancy engineering or doping, while maintaining conductivity and structural stability under harsh conditions, as well as optimizing adsorption and desorption of key intermediates. The scalability of synthesis also remains restricted, and long-term durability at industrially relevant current densities is rarely demonstrated, raising questions about practical viability. Addressing these obstacles includes lowering overpotentials to match noble metals, achieving precise termination engineering, ensuring oxidation resistance and structural stability, and developing

green, scalable production methods, which will be essential for consistent performance in extended operation.

Based on the current state of the art and the requirement for scalability and cost-effectiveness, three directions stand out: first, surface engineering, such as surface termination, doping, or creating vacancies, that can better control adsorption and reactivity; second, advancing single-atom and dual-atom catalysis, ideally using earth-abundant elements for scalability while taking advantage of the unique properties of noble and transition metals; third, employing *operando* tools such as XAS, Raman, and XPS to track active sites under working conditions to verify the mechanism during the reaction. Synergetic ideas such as heterostructures, surface engineering, and surface anchoring are highly recommended to address electrocatalysts for specific cases and expand their applications. Alongside these, long-term durability tests and greener, scalable synthesis methods will be key for practical deployment.

In short, $Ti_3C_2T_x$ has proven itself as a versatile scaffold for electrocatalytic applications such as the HER, OER, and CO_2RR, where atomic-level design strategies already deliver impressive results. The next breakthroughs will come from mastering stability, termination control, and scalability, moving MXene-based catalysts from the lab toward real applications in sustainable energy conversion.

Conflicts of interest

The authors declare that they have no competing financial interests or personal relationships that could have influenced the work reported in this study.

Data availability

No new data were created or analyzed in this study. All data supporting the findings of this work are available within the published literature cited throughout the manuscript.

References

1 S. Emiliozzi, F. Ferriani and A. Gazzani, *Energy J.*, 2025, **46**, 119–145.

2 J. J. Szczygielski, A. Charteris, L. Obojska and J. Brzeszczyński, *Int. Rev. Financ. Anal.*, 2025, **104**, 103838.

3 Y. Yao, X. Rui, R. Bai, Y. Ouyang, G. Li, Y. Zhao, Y.-H. Zhu, M. Zhao, B.-Q. Li, X. Zhang, *et al.*, *ACS Nano*, 2025, **19**, 10091.

4 F. Wang, L. Xiao, Y. Jiang, X. Liu, X. Zhao, Q. Kong, A. Abdukayum and G. Hu, *Mater. Horiz.*, 2025, **12**, 1757–1795.

5 C. C. Wang, Z. S. Guo, Q. Shen, Y. R. Xu, C. P. Lin, X. D. Yang, C. C. Li, Y. Q. Sun and L. F. Hang, *Rare Met.*, 2025, **44**, 2180–2207.

6 N. T. Padmanabhan, L. Clarizia and P. Ganguly, *Curr. Opin. Chem. Eng.*, 2025, **48**, 101135.

7 S. M. Parsa, Z. Chen, H. H. Ngo, W. Wei, X. Zhang, Y. Liu, B. J. Ni and W. Guo, *Nano-Micro Lett.*, 2025, **17**, 1–62.

8 M. K. Wong, J. Y. Loh, F. M. Yap and W. J. Ong, *InfoMat*, 2025, **7**, e12639.

9 J. Chen, W. Zhang, R. Chen, Y. Dai, J. Zhang, H. Yang, W. Zong, Z. Jiang, Y. Zhong, J. Wang, X. Zhang and G. He, *Adv. Energy Mater.*, 2025, **15**, 2403757.

10 H. Yuan, J. Hua, W. Wei, M. Zhang, Y. Hao and J. Chang, *Carbon Energy*, 2025, **7**, e639.

11 S. Gokul Eswaran, M. Rashad, A. Santhana Krishna Kumar and A. F. M. El-Mahdy, *Chem.–Asian J.*, 2025, **20**, e202401181.

12 R. Ali, M. Islam, M. Shafi, S. Ali and H. E. Wang, *Coord. Chem. Rev.*, 2025, **540**, 216797.

13 S. P. Vinodhini and J. R. Xavier, *J. Mater. Sci.*, 2025, **60**, 1–43.

14 M. Naguib, M. Kurtoglu, V. Presser, J. Lu, J. Niu, M. Heon, L. Hultman, Y. Gogotsi and M. W. Barsoum, *Adv. Mater.*, 2011, **23**, 4248–4253.

15 K. Shevchuk, T. Hryhorchuk, Y. Zhang and Y. Gogotsi, *ECS Meet. Abstr.*, 2025, **MA2025-01**, 1121.

16 K. Diedkova, I. Roslyk, N. Kanas, L. Grine, V. Deineka, A. Blacha-Grzechnik, M. Boroduskis, I. Iatsunskyi, B. Ej Anastaziak, A. Konieva, *et al.*, *ACS Appl. Mater. Interfaces*, 2025, **17**, 47919–47937.

17 N. M. Tran, Q. T. H. Ta and J.-S. Noh, *Appl. Surf. Sci.*, 2021, **538**, 148023.

18 N. M. Tran, Q. T. H. Ta, A. Sreedhar and J.-S. Noh, *Appl. Surf. Sci.*, 2021, **537**, 148006.

19 N. Talreja, M. Ashfaq, D. Chauhan and R. V. Mangalaraja, *Mater. Chem. Phys.*, 2023, **294**, 127029.

20 Z. Yen, T. Salim, C. Boothroyd, P. F. Haywood, C. T. Kuo, S. J. Lee, J. S. Lee, D. Y. Cho and Y. M. Lam, *ACS Appl. Nano Mater.*, 2023, **6**, 16486–16496.

21 Z. Xu, Y. Chen, Q. Meng, A. Yang, H. Zhang and G. Zhang, *Nanotechnology*, 2024, **35**, 125604.

22 W. Zhang, J. Zhang, Y. Li and X. Yang, *Ceram. Int.*, 2020, **46**, 15492–15501.

23 K. Mahabari, M. Patel, R. D. Mohili, A. H. Jadhav and N. K. Chaudhari, *ACS Appl. Eng. Mater.*, 2025, **3**, 1012–1023.

24 T. L. Khang and J. Bae, *Polymers*, 2025, **17**, 3109.

25 X. Sun, X. Luo, X. Li, S. Li and X. Zhao, *ACS Appl. Nano Mater.*, 2025, **8**, 22501–22517.

26 Z. Song, S. Fan, Z. Cui, W. Peng, Z. Wang and J. Liu, *Small*, 2025, e09924.

27 Q. T. H. Ta, M. Jianbin, N. Thi Chau, N. Hoi Nguyen, D. Linh Tran, T. M. Huyen Nguyen, M. Hoang Tran, V.-Q. Hoang, S. Seo and D. Hai Nguyen, *Nanoscale Adv.*, 2025, **7**, 3999–4017.

28 Q. T. H. Ta, D. Thakur and J.-S. Noh, *Chemosensors*, 2023, **11**, 477.

29 M. Misra, A. Sreedhar and J. S. Noh, *Microchem. J.*, 2025, **216**, 114632.

30 Q. T. H. Ta, A. Sreedhar, N. N. Tri and J.-S. Noh, *Ceram. Int.*, 2024, **50**, 27227–27236.

31 V. T. T. Linh, N. P. T. Trieu, Q. T. H. Ta, N. N. Tri, V. N. Huynh, D. T. Y. Oanh, N. H. Hieu and S. Seo, *Vietnam J. Chem.*, 2026, **1**, DOI: 10.1002/vjch.70129.

32 L. T. Nhiem, J. Mao, Q. T. Hoai Ta and S. Seo, *Nanoscale Adv.*, 2025, **7**, 1452–1463.

33 N. Shpigel, A. Chakraborty, F. Malchik, G. Bergman, A. Nimkar, B. Gavriel, M. Turgeman, C. N. Hong, M. R. Lukatskaya, M. D. Levi, Y. Gogotsi, D. T. Major and D. Aurbach, *J. Am. Chem. Soc.*, 2021, **143**, 12552–12559.

34 M. A. Munir and S. Khalid, *Energy Fuels*, 2025, **39**, 2889–2915.

35 H. Zhong, H. Fang, Z. Yan and F. Wu, *Polym. Eng. Sci.*, 2025, **65**, 2513–2524.

36 Y. M. Wei, K. D. Kumar, L. Zhang and J. F. Li, *Front. Chem.*, 2025, **13**, 1636683.

37 L. Fei, L. Lei, H. Xu, X. Guo, B. Chen, X. Han, X. Chen, Q. Huang and D. Wang, *Carbon Energy*, 2025, **7**, e678.

38 T. H. Han, H. Shin, W. Eom, K. H. Lee, W. Jeong and D. J. Kang, *ACS Nano*, 2021, **15**, 3320–3329.

39 K. Maleski, C. E. Ren, M. Q. Zhao, B. Anasori and Y. Gogotsi, *ACS Appl. Mater. Interfaces*, 2018, **10**, 24491–24498.

40 V. Natu and M. W. Barsoum, *J. Phys. Chem. C*, 2023, **127**, 20197–20206.

41 E. Pranada, B. Ngozichukwu, R. Yoo, D. Johnson, M. A. Barteau, A. Abdel-Wahab and A. Djire, *ACS Catal.*, 2025, **15**, 982–991.

42 S. K. Kailasa, D. J. Joshi, J. R. Koduru and N. I. Malek, *J. Mol. Liq.*, 2021, **342**, 117524.

43 A. Sreedhar and J. S. Noh, *Nanomaterials*, 2025, **15**, 673.

44 M. P. Bilibana, *Adv. Sens. Energy Mater.*, 2023, **2**, 100080.

45 X. H. Zha, K. Luo, Q. Li, Q. Huang, J. He, X. Wen and S. Du, *Europhys. Lett.*, 2015, **111**, 26007.

46 U. Shahzad, H. M. Marwani, M. Saeed, A. M. Asiri and M. M. Rahman, *ChemistrySelect*, 2023, **8**, e202300737.

47 D. M. Saju, R. Sapna, U. Deka and K. Hareesh, *J. Power Sources*, 2025, **647**, 237302.

48 B. Anasori, C. Shi, E. J. Moon, Y. Xie, C. A. Voigt, P. R. C. Kent, S. J. May, S. J. L. Billinge, M. W. Barsoum and Y. Gogotsi, *Nanoscale Horiz.*, 2016, **1**, 227–234.

49 M. Mariano, O. Mashtalir, F. Q. Antonio, W. H. Ryu, B. Deng, F. Xia, Y. Gogotsi and A. D. Taylor, *Nanoscale*, 2016, **8**, 16371–16378.

50 R. A. Soomro, P. Zhang, B. Fan, Y. Wei and B. Xu, *Nano-Micro Lett.*, 2023, **15**, 1–18.

51 Y. Wu, X. Li, H. Zhao, F. Yao, J. Cao, Z. Chen, X. Huang, D. Wang and Q. Yang, *Chem. Eng. J.*, 2021, **418**, 129296.

52 T. Habib, X. Zhao, S. A. Shah, Y. Chen, W. Sun, H. An, J. L. Lutkenhaus, M. Radovic and M. J. Green, *npj 2D Mater. Appl.*, 2019, **3**, 1–6.

53 Q. Zhang, H. Lai, R. Fan, P. Ji, X. Fu and H. Li, *ACS Nano*, 2021, **15**, 5249–5262.

54 X. Zhao, A. Vashisth, E. Prehn, W. Sun, S. A. Shah, T. Habib, Y. Chen, Z. Tan, J. L. Lutkenhaus, M. Radovic and M. J. Green, *Matter*, 2019, **1**, 513–526.

55 V. Natu, J. L. Hart, M. Sokol, H. Chiang, M. L. Taheri and M. W. Barsoum, *Angew. Chem., Int. Ed.*, 2019, **58**, 12655–12660.

56 Y. Xie and P. R. C. Kent, *Phys. Rev. B: Condens. Matter Mater. Phys.*, 2013, **87**, 235441.

57 M. Khazaei, A. Mishra, N. S. Venkataramanan, A. K. Singh and S. Yunoki, *Curr. Opin. Solid State Mater. Sci.*, 2019, **23**, 164–178.

58 M. Naguib, V. N. Mochalin, M. W. Barsoum and Y. Gogotsi, *Adv. Mater.*, 2014, **26**, 992–1005.

59 K. Khan, A. K. Tareen, W. Ahmad, I. Hussain, M. U. Chaudhry, A. Mahmood, M. F. Khan, H. Zhang and Z. Xie, *Adv. Sci.*, 2024, **11**, 2303998.

60 J. Chen, X. Gao, J. Li, Z. Kang, J. Bai, T. Wang, Y. Yuan, C. You, Y. Chen, B. Y. Xia and X. Tian, *Electron*, 2024, **2**(1), 17.

61 W. Zhou, Z. Yu, Y. Zhao, T. Zhi and L. Wang, *J. Alloys Compd.*, 2025, **1036**, 181615.

62 T. L. Khang and J. Bae, *Polymers*, 2025, **17**, 2828.

63 J. He, J. D. Butson, R. Gu, A. C. M. Loy, Q. Fan, L. Qu, G. K. Li and Q. Gu, *Adv. Sci.*, 2025, **12**, 2414674.

64 X. Bai and J. Guan, *Small Struct.*, 2023, **4**, 2200354.

65 S. Yang, P. Zhang, F. Wang, A. G. Ricciardulli, M. R. Lohe, P. W. M. Blom and X. Feng, *Angew. Chem., Int. Ed.*, 2018, **57**, 15717–15721.

66 V. H. Nguyen, B. S. Nguyen, C. Hu, C. C. Nguyen, D. L. T. Nguyen, M. T. N. Dinh, D. V. N. Vo, Q. T. Trinh, M. Shokouhimehr, A. Hasani, S. Y. Kim and Q. Van Le, *Nanomaterials*, 2020, **10**, 602.

67 Y. Cai, X. Chen, Y. Xu, Y. Zhang, H. Liu, H. Zhang and J. Tang, *Carbon Energy*, 2024, **6**, 501.

68 S. Bai, M. Yang, J. Jiang, X. He, J. Zou, Z. Xiong, G. Liao and S. Liu, *npj 2D Mater. Appl.*, 2021, **5**, 59.

69 L. Huang, T. Li, Q. Liu and J. Gu, *Electrochem. Commun.*, 2019, **103**, 106475.

70 A. Patra, R. Samal and C. S. Rout, *Catal. Today*, 2023, **404**, 69–78.

71 F. Guo, T. J. Macdonald, A. J. Sobrido, L. Liu, J. Feng and G. He, *Adv. Sci.*, 2023, **10**, 2301098.

72 L. Meng, L. K. Yan, F. Viñes and F. Illas, *J. Mater. Chem. A*, 2023, **11**, 6886–6900.

73 W. Sun, Y. Wang, K. Xiang, S. Bai, H. Wang, J. Zou, Arramel and J. Jiang, *Acta Phys.-Chim. Sin.*, 2023, **39**, 308015.

74 W. Guo, B. Wang and Q. Shu, *Metals*, 2024, **14**, 922.

75 X. Liu, X. Chen, C. Huang, S. Sun, D. Yuan and Y. Dou, *Catalysts*, 2025, **15**, 663.

76 M. A. Tekalgne, H. H. Do, T. Van Nguyen, Q. Van Le, J. An, S. H. Hong, S. H. Ahn, H. Kang, J. S. Kim and S. Y. Kim, *Int. J. Energy Res.*, 2023, **2023**, 8980888.

77 Y. Jiang, T. Sun, X. Xie, W. Jiang, J. Li, B. Tian and C. Su, *ChemSusChem*, 2019, **12**, 1368–1373.

78 A. D. Handoko, K. D. Fredrickson, B. Anasori, K. W. Convey, L. R. Johnson, Y. Gogotsi, A. Vojvodic and Z. W. Seh, *ACS Appl. Energy Mater.*, 2018, **1**, 173–180.

79 Y. Zou, S. A. Kazemi, G. Shi, J. Liu, Y. Yang, N. M. Bedford, K. Fan, Y. Xu, H. Fu, M. Dong, M. Al-Mamun, Y. L. Zhong, H. Yin, Y. Wang, P. Liu and H. Zhao, *EcoMat*, 2023, **5**, e12274.

80 J. Zhang, E. Wang, S. Cui, S. Yang, X. Zou and Y. Gong, *Nano Lett.*, 2022, **22**, 1398–1405.

81 J. Li, *Nano-Micro Lett.*, 2022, **14**, 3.

82 X. Liu, Z. He, M. Ajmal, C. Shi, R. Gao, L. Pan, Z. F. Huang, X. Zhang and J. J. Zou, *Trans. Tianjin Univ.*, 2023, **29**, 247–253.

83 M. J. Craig, G. Coulter, E. Dolan, J. Soriano-López, E. Mates-Torres, W. Schmitt and M. García-Melchor, *Nat. Commun.*, 2019, **10**, 4994.

84 J. Sheng, J. Kang, P. Jiang, K. Meinander, X. Hong, H. Jiang, Nonappa, O. Ikkala, H. P. Komsa, B. Peng and Z. P. Lv, *Small*, 2025, **21**(3), 2404927.

85 G. Schröder, S. Sajjadi, B. Schmiedecke, A. A. Emerenciano, T. Schultz, N. Koch, M. Buldu-Akturk and M. P. Browne, *ChemElectroChem*, 2025, **12**, e202400656.

86 M. Bhosale, S. Thangarasu, N. Murugan, Y. A. Kim and T. H. Oh, *ChemSusChem*, 2025, **18**, e202402603.

87 Y. Yan, B. Y. Xia, B. Zhao and X. Wang, *J. Mater. Chem. A*, 2016, **4**, 17587–17603.

88 P. Zhang, R. Wang, T. Xiao, Z. Chang, Z. Fang, Z. Zhu, C. Xu, L. Wang and J. Cheng, *Energy Technol.*, 2020, **8**, 2000306.

89 D. Guo, X. Li, Y. Jiao, H. Yan, A. Wu, G. Yang, Y. Wang, C. Tian and H. Fu, *Nano Res.*, 2022, **15**, 238–247.

90 B. Sarfraz, M. T. Mehran, F. Shahzad, S. Hussain, S. R. Naqvi, H. A. Khan and K. Mahmood, *RSC Adv.*, 2023, **13**, 22017–22028.

91 S. Hussain, D. Vikraman, G. Nazir, M. T. Mehran, F. Shahzad, K. M. Batoo, H. S. Kim and J. Jung, *Nanomaterials*, 2022, **12**, 2886.

92 K. Yu, J. Zhang, Y. Hu, L. Wang, X. Zhang and B. Zhao, *Catalysts*, 2024, **14**, 184.

93 S. Ligani Fereja, A. Mehmood, Q. Ji, W. Raza, A. Hussen, J. Hu, S. Zhai and X. Cai, *InfoMat*, 2025, **7**(1), e12623.

94 S. Jiang, H. Suo, T. Zhang, C. Liao, Y. Wang, Q. Zhao and W. Lai, *Catalysts*, 2022, **12**, 123.

95 E. Enkhtuvshin, S. Yeo, H. Choi, K. M. Kim, B. S. An, S. Biswas, Y. Lee, A. K. Nayak, J. U. Jang, K. H. Na, W. Y. Choi, G. Ali, K. H. Chae, M. Akbar, K. Y. Chung, K. Yoo, Y. C. Chung, T. H. Shin, H. Kim, C. Y. Chung and H. S. Han, *Adv. Funct. Mater.*, 2023, **33**(22), 2214069.

96 J. Wang, Y. Liu, G. Yang, Y. Jiao, Y. Dong, C. Tian, H. Yan and H. Fu, *Nat. Commun.*, 2025, **16**, 1319.

97 K. Farooq, Z. Yang, M. Murtaza, M. A. Naseeb, A. Waseem, Y. Zhu and Y. Xia, *Adv. Energy Sustain. Res.*, 2025, **6**, 2400400.

98 A. Irfan, I. Ullah, M. Li, W. Xu, Z. Dong, H. Zhao, H. Hu, N. Irshad, K. Yang, P. Zhong and P. K. Chu, *Surf. Interfaces*, 2025, **56**, 105536.

99 J. Su, Y. Song and R. Ye, *Chem Catal.*, 2024, **4**, 101026.

100 H. Bao, Y. Qiu, X. Peng, J. Wang, Y. Mi, S. Zhao, X. Liu, Y. Liu, R. Cao, L. Zhuo, J. Ren, J. Sun, J. Luo and X. Sun, *Nat. Commun.*, 2021, **12**, 3364.

101 Y. Yan, D. Sall, L. Loupias, S. Célérier, M. Aouine, P. Bargiela, M. Prévot, F. Morfin and L. Piccolo, *Mol. Catal.*, 2023, **548**, 100010.

102 S. Krishnan, S. Marimuthu, M. K. Singh and D. K. Rai, *Energy Adv.*, 2023, **2**, 1166–1175.

103 R. Nittoor-Veedu, X. Ju, M. Langer, W. Gao, M. Otyepka and M. Pumera, *Small*, 2025, **21**, 2410105.

104 S. Pablo Lozano-Reis and K. S. Exner, *Mater. Horiz.*, 2025, **12**, 4662.

105 N. Jeyachandran, W. Yuan and C. Giordano, *Molecules*, 2023, **28**, 3504.

106 L. Meng, L. K. Yan, F. Viñes and F. Illas, *J. Mater. Chem. A*, 2024, **12**, 6886–6900.

107 S. A. Talas, S. El-Hout, F. M. Alissa, J. K. El-Demellawi, P. Castaño, H. Mohamed, P. D. Kolubah, R. Khairova and M. Alqahtani, *Mater. Horiz.*, 2025, **12**, 4662–4686.

108 L. Han, X. Peng, H. T. Wang, P. Ou, Y. Mi, C. W. Pao, J. Zhou, J. Wang, X. Liu, W. F. Pong, J. Song, Z. Lin, J. Luo and H. L. Xin, *Proc. Natl. Acad. Sci. U. S. A*, 2022, **119**, e2207326119.

109 M. Abdinejad, S. Subramanian, K. Motlagh, M. Noroozifar, S. Duangdangchote, I. Neporozhnii, D. Ripepi, D. Pinto, M. Li, K. Tang, J. Middelkoop, A. Urakawa, O. Voznyy, T. Burdyny and H.-B. Kraatz, *Adv. Energy Mater.*, 2023, **13**, 2300402.

110 Q. Zhao, C. Zhang, R. Hu, Z. Du, J. Gu, Y. Cui, X. Chen, W. Xu, Z. Cheng, S. Li, B. Li, Y. Liu, W. Chen, C. Liu, J. Shang, L. Song and S. Yang, *ACS Nano*, 2021, **15**, 4927–4936.

111 Y. Wang, Y. Sun, H. Li, W. Zhang, S. Wu, C. Liu, Y. Gao, B. Jia, J. Qiu, T. Ma and C. Y. Sun, *Carbon Neutrality*, 2022, **1**, 117–125.

112 S. G. Peera, C. Liu, A. K. Sahu, M. Selvaraj, M. C. Rao, T. G. Lee, R. Koutavarapu, J. Shim and L. Singh, *Adv. Mater. Interfaces*, 2021, **8**, 2100975.

113 J. Wang, M. Liu, H. Zhang, C. Du, S. Yang, Y. Gong and X. Zou, *Nano Lett.*, 2019, **19**, 6427–6434.

114 Y. Wang, H. Liu, Z. Wang, Z. Yang, X. Liu, C. Wang and S. Han, *Chem. Eng. J.*, 2022, **446**, 137256.